

1 **The impact of volcanic aerosol on the Northern Hemisphere stratospheric polar**  
2 **vortex: mechanisms and sensitivity to forcing structure**

3

4 Matthew Toohey<sup>1</sup>, Kirstin Krüger<sup>1,2</sup>, Matthias Bittner<sup>3,4</sup>, Claudia Timmreck<sup>3</sup>, Hauke Schmidt<sup>3</sup>

5

6 [1] {GEOMAR Helmholtz Centre for Ocean Research Kiel, Kiel, Germany}

7 [2] {University of Oslo, Department of Geosciences, Oslo, Norway}

8 [3] {Max Planck Institute for Meteorology, Hamburg, Germany}

9 [4] {International Max Planck Research School on Earth System Modeling (IMPRS), Hamburg, Germany}

10

11 Correspondence to: Matthew Toohey (mtoohey@geomar.de)

12

13 **Abstract**

14

15 Observations and simple theoretical arguments suggest that the Northern Hemisphere (NH)  
16 stratospheric polar vortex is stronger in winters following major volcanic eruptions. However, recent  
17 studies show that climate models forced by prescribed volcanic aerosol fields fail to reproduce this  
18 effect. We investigate the impact of volcanic aerosol forcing on stratospheric dynamics, including the  
19 strength of the NH polar vortex, in ensemble simulations with the Max Planck Institute Earth System  
20 Model. The model is forced by four different prescribed forcing sets representing the radiative  
21 properties of stratospheric aerosol following the 1991 eruption of Mt. Pinatubo: two forcing sets are  
22 based on observations, and are commonly used in climate model simulations, and two forcing sets are  
23 constructed based on coupled aerosol-climate model simulations. For all forcings, we find that  
24 temperature and zonal wind anomalies in the NH high latitudes are not directly impacted by anomalous  
25 volcanic aerosol heating. Instead, high latitude effects result from enhancements in stratospheric  
26 residual circulation, which in turn result, at least in part, from enhanced stratospheric wave activity.  
27 High latitude effects are therefore much less robust than would be expected if they were the direct  
28 result of aerosol heating. Both observation-based forcing sets result in insignificant changes in vortex  
29 strength. For the model-based forcing sets, the vortex response is found to be sensitive to the structure  
30 of the forcing, with one forcing set leading to significant strengthening of the polar vortex in rough  
31 agreement with observation-based expectations. Differences in the dynamical response to the forcing  
32 sets imply that reproducing the polar vortex responses to past eruptions, or predicting the response to  
33 future eruptions, depends on accurate representation of the space-time structure of the volcanic  
34 aerosol forcing.

35

36 **1. Introduction**

37

38 The Northern Hemisphere (NH) stratospheric winter polar vortex, which shows considerable interannual  
39 and intra-seasonal variability, has been observed to be stronger than normal in winters after major  
40 volcanic eruptions (Kodera, 1995; Labitzke and van Loon, 1989). While this observation is based on a  
41 relatively small sample (limited to the winters after the 1963 Agung, 1982 El Chichón and 1991 Pinatubo  
42 eruptions), the theoretical argument to explain such a strengthening appears clear: namely, that heating  
43 of the lower stratosphere through the absorption of radiation by volcanic sulfate aerosols enhances the  
44 equator-to-pole temperature gradient in the lower stratosphere, which, through the thermal wind  
45 equation, leads to stronger westerly winds (Robock, 2000 and references therein). Satellite observations  
46 clearly show a warming of the tropical lower stratosphere after volcanic eruptions (Labitzke and  
47 McCormick, 1992), so changes in meridional temperature gradients and zonal winds are logical  
48 consequences. The degree to which secondary feedback mechanisms -- such as changes in ozone or  
49 upward propagating planetary waves (e.g., Graf et al., 2007; Stenchikov et al., 2006)-- also affect the  
50 vortex strength is at present unclear.

51

52 Post-volcanic strengthening of the NH polar vortex is an important step in a proposed mechanism which  
53 explains observed changes in surface climate in post-eruption winters (Kodera, 1994; Perlwitz and Graf,  
54 1995). Specifically, it is thought that through stratosphere-troposphere coupling (Baldwin and  
55 Dunkerton, 2001; Gerber et al., 2012) the volcanically-induced strong stratospheric polar vortex leads to  
56 the observed positive anomalies in surface dynamical indexes such as the Northern Annular Mode  
57 (NAM) or North Atlantic Oscillation (NAO) (Christiansen, 2008). Such dynamical changes lead to the  
58 “winter warming” pattern of post-volcanic temperature anomalies (Robock and Mao, 1992), which is  
59 characterized by warmer temperatures over large regions of the NH continents during winter which  
60 oppose the overall cooling impact of the volcanic aerosols on the surface. On the other hand, in a model  
61 study, Stenchikov (2002) found that a positive phase of the NAM was also produced in an experiment in  
62 which only the tropospheric impact of volcanic aerosols was included, implying that aerosol heating in  
63 the lower tropical stratosphere is not necessary to force a positive NAM response. Whatever the  
64 mechanisms, observations show that 11 out of 13 eruptions since 1870 were followed by positive  
65 wintertime NAO values (Christiansen, 2008): the apparent robustness of this post-eruption dynamical  
66 response should allow for enhanced skill in seasonal prediction for winters which follow volcanic  
67 eruptions (e.g., Marshall et al., 2009).

68

69 While a number of early model simulations reported qualified success in simulating the atmospheric  
70 dynamical response to volcanic eruptions (e.g., Graf et al., 1993; Kirchner et al., 1999; Rozanov, 2002;  
71 Shindell et al., 2001), assessments of the multi-model ensembles of the Coupled Model Intercomparison  
72 Projects (CMIP) 3 and 5 showed no significant winter warming response to prescribed volcanic forcing,  
73 nor did they show significant anomalies in post-eruption dynamical quantities in the stratosphere or at  
74 the surface (Driscoll et al., 2012; Stenchikov et al., 2006). It has been suggested that in order for a model  
75 to successfully respond to volcanic forcing, it should include a reasonably well-resolved stratosphere  
76 (Shindell, 2004; Stenchikov et al., 2006). However, analysis of the CMIP5 ensemble revealed no  
77 appreciable systematic difference in post-eruption geopotential height anomalies to volcanic aerosol  
78 forcing between models with or without well-resolved stratospheres (Charlton-Perez et al., 2013).

79

80 Most model simulations which incorporate the impact of volcanic eruptions, such as the CMIP3 and 5  
81 historical simulations, do so using prescribed volcanic aerosol fields, which have associated  
82 uncertainties. In this study we investigate how the response of the atmosphere to volcanic aerosol  
83 forcing depends on the prescribed aerosol forcing used in the simulation. We use one CMIP5 model, the  
84 MPI-ESM, and focus on the first winter after Mt. Pinatubo, the period of strongest volcanic forcing  
85 within the era of satellite observations. We run ensemble simulations using four different forcing data  
86 sets: two observation-based forcing sets, based primarily on different versions of SAGE II aerosol  
87 extinction measurements, and two model-constructed aerosol forcing sets. By assessing the model  
88 response to these forcing sets, we investigate (1) the mechanisms linking volcanic aerosol heating in the  
89 lower tropical stratosphere and NH winter vortex strength, (2) what stratospheric circulation responses  
90 to volcanic aerosol forcing are robustly produced by the model and forcings, and (3) the sensitivity of  
91 the vortex response to changes in the space-time structure of the volcanic forcing.

92

## 93 **2 Experiment: Observational basis, model and methods**

94 In this section, the hypothesis that volcanic eruptions produce a strengthened NH winter polar vortex is  
95 briefly summarized by examining ERA-interim reanalysis data. Then, the materials and methods of the  
96 present modelling study are presented including the model and volcanic forcing sets used, and the  
97 design of the ensemble simulations and analysis.

### 98 **2.1 NH polar vortex response to volcanic eruptions in ERA-interim**

99

100 The NH polar vortex is highly variable as a result of unforced internal variability, and the impact of  
101 external forcings such as volcanic eruptions, the 11-year solar cycle, the El Niño Southern Oscillation  
102 (ENSO), and the QBO. Isolating the vortex response to any individual forcing term can be difficult,  
103 especially in the case of major volcanic eruptions for which so few actual events have occurred within  
104 the era of satellite measurements.

105  
106 A common and simple method to isolate the pure volcanic impact on the state of the NH winter  
107 stratosphere is to simply average post-eruptive anomalies over winters after recent major volcanic  
108 eruptions. This technique is here applied to ERA-Interim reanalysis (Dee et al., 2011) temperature and  
109 zonal wind fields after the eruptions of El Chichón (1982) and Pinatubo (1991). Post-eruption winter  
110 anomalies are constructed for the two winters after each eruption by differencing post-eruptive  
111 December-to-February (DJF) mean fields with fields averaged for 3 (El Chichón) and 5 (Pinatubo) years  
112 before the eruption (the shorter reference period for El Chichón resulting from the fact that the ERA-  
113 Interim data set begins in 1979). Differences in post-eruption anomalies for Pinatubo are not strongly  
114 dependent on the choice of a 3, 4 or 5 year reference period.

115  
116 Figure 1 (left) shows ERA-Interim temperature and zonal wind anomalies composited for 4 winters, the 2  
117 winters each after Pinatubo and El Chichón. Mean temperature anomalies in the post-volcanic  
118 composite show positive anomalies in the tropical lower stratosphere, as would be expected due to  
119 aerosol heating. Temperature anomalies also show cooling of the tropical upper stratosphere, cooling of  
120 the NH polar lower stratosphere, and warming of the NH polar upper stratosphere. Mean post-volcanic  
121 zonal winds show a strengthening of the NH winter polar vortex by  $\sim 6$  m/s. Such a simple average with a  
122 small sample size does not completely remove the influences of variability resulting from other forcing  
123 terms—notably the solar activity was at a maximum at the times of both the El Chichón and Pinatubo  
124 eruptions, and El Niño events were observed in the first winters after both eruptions—but the  
125 composite temperature and zonal wind anomaly structure is certainly a better approximation of the  
126 direct volcanic impact than anomalies in any single post-volcanic year. For comparison, single winter  
127 anomalies are shown for the first winter after the Pinatubo eruption. Temperature anomalies for DJF  
128 1991/92 roughly follow the structure of the 4-year composite, albeit with tropical positive anomalies  
129 located at higher altitudes, and weaker polar lower stratosphere cooling. Post-Pinatubo zonal wind  
130 anomalies in the tropics reflect the state of the QBO at the time, with negative (easterly) wind  
131 anomalies in the middle stratosphere ( $\sim 50$ -15 hPa) and positive (westerly) anomalies in the upper

132 stratosphere (15-2 hPa). The polar vortex in the first post-Pinatubo winter was actually not as clearly  
133 enhanced as the 4-year composite, with positive zonal wind anomalies only in the mid to lower polar  
134 stratosphere centered at  $\sim 70^\circ\text{N}$ . It is likely that in addition to the volcanic forcing, the vortex in DJF  
135 1991/92 was weakened somewhat due to the influences of the concurrent forcing of the El Niño and  
136 QBO easterly phase. Based on these arguments, it can be hypothesized that the pure response of the  
137 stratosphere to Pinatubo aerosol forcing would have the approximate structure of the composite  
138 response shown in Fig. 1 (left), albeit with greater amplitude, since the aerosol optical depth and hence  
139 aerosol radiative heating during the first post-Pinatubo winter is the strongest of the years used in the  
140 volcanic composite. This “expected” response in the first post-Pinatubo winter is based on a small  
141 sample size of observations, and an assumption of linear response to the magnitude of volcanic forcing,  
142 however, in light of limited evidence, it represents a best first-order, observation-based expectation,  
143 consistent with that assumed explicitly or implicitly in prior studies.

144

## 145 **2.2 MPI-ESM**

146

147 The MPI-ESM is a full Earth System model, with atmosphere, ocean, carbon cycle, and vegetation  
148 components. Major characteristics of the full ESM and its performance in the CMIP5 experiments are  
149 described by Giorgetta et al. (2013). The “low resolution” model configuration (MPI-ESM-LR) is used  
150 here, with horizontal resolution of the atmospheric component given by a triangular truncation at 63  
151 wave numbers (T63) and 47 vertical layers extending to 0.01 hPa. Unlike model configurations with  
152 higher vertical resolutions, the LR version has no internally generated Quasi Biennial Oscillation (QBO).

153

154 CMIP5 historical simulations have previously been performed with the MPI-ESM model over the time  
155 period 1850-2005. Prescribed external forcings for the historical simulations, including volcanic aerosols  
156 as well as greenhouse gases and ozone follow CMIP5 recommendations, and the responses to these  
157 forcings are described by Schmidt et al. (2013).

158

159 The MPI-ESM is configured to take volcanic aerosol forcing data in two formats, both of which are used  
160 in this study. One format consists of monthly zonal mean values of aerosol extinction, single scattering  
161 albedo, and asymmetry factor as a function of time, pressure, and the 30 short wave and long wave  
162 spectral bands used by the model. This format is consistent with the observation-based forcings sets  
163 introduced in Sec 2.3. A second format consists of monthly zonal mean aerosol extinction at  $0.55 \mu\text{m}$ ,

164 and zonal mean effective radius, both as a function of latitude, height, and time. Pre-calculated look-up  
165 tables are then used to scale the 0.55  $\mu\text{m}$  extinction to the wavelengths of the model's radiation code  
166 based on the effective radius. This methodology has been used to perform MPI-ESM simulations using  
167 the forcing timeseries of Crowley et al. (2008, e.g., Timmreck et al., 2009) or output from prior runs of  
168 the MAECHAM5-HAM coupled aerosol-climate model, (e.g., Timmreck et al., 2010) as done in this study  
169 and described in Sec 2.4.

170

### 171 **2.3 Observation-based aerosol forcing sets**

172

173 Volcanic sulfate aerosol forcing for the MPI-ESM CMIP5 historical simulations is based on an extended  
174 version of the aerosol data set developed by Stenchikov et al. (1998, hereafter S98) on the basis of SAGE  
175 II measurements of aerosol extinction at 1.02  $\mu\text{m}$  and estimates of effective radii derived from  
176 instruments on the Upper Atmosphere Research Satellite. The data are given at 40 pressure levels and  
177 interpolated to the actual hybrid model layers during the simulations. The S98 data set is based  
178 primarily on retrievals of aerosol extinction at 1.02  $\mu\text{m}$  from SAGE II, with gaps filled with data from  
179 ground-based lidar systems. Together, the S98 forcing set and that from Sato et al., (1993, with updates  
180 <http://data.giss.nasa.gov/modelforce/strataer/>), both primarily based on SAGE II data, have been used  
181 in roughly half of the models that performed CMIP5 historical simulations (Driscoll et al., 2012).

182

183 Subsequent updates to the SAGE II retrievals have led to significant changes in the space-time  
184 morphology of the estimated aerosol extinction after Pinatubo (Arfeuille et al., 2013; Thomason and  
185 Peter, 2006). A new volcanic forcing set (SAGE\_4 $\lambda$ , Arfeuille et al., 2013) has been compiled and made  
186 available to modeling centers ([http://www.pa.op.dlr.de/CCMI/CCMI\\_SimulationsForcings.html](http://www.pa.op.dlr.de/CCMI/CCMI_SimulationsForcings.html)),  
187 specifically for use in Chemistry climate simulations within the Chemistry Climate Model  
188 Intercomparison (CCMI) initiative (Eyring and Lamarque, 2013). Timeseries of zonal mean aerosol optical  
189 depth (AOD) at 1  $\mu\text{m}$ —the wavelength closest to the original SAGE II measurements and so less impacted  
190 by uncertainties in derived aerosol size distribution—are shown in Fig. 2 over the Pinatubo period for  
191 the S98 and SAGE\_4 $\lambda$  reconstructions.

192

193 It should be noted that even for Pinatubo—the best-observed eruption in history—the observation-  
194 based volcanic aerosol forcing sets suffer from significant but mostly unquantified uncertainties. Most  
195 notably, gaps in the satellite record result from sparse sampling of the satellite instruments (Stenchikov

196 et al., 1998) and the fact that large optical depths in the initial months after the Pinatubo eruption  
197 reduced atmospheric transmission below detectability (Russell et al., 1996).

198

#### 199 **2.4 Model-based aerosol forcing sets**

200

201 Two “synthetic” volcanic aerosol forcing sets were constructed based on a 12-member ensemble of  
202 simulations of a Pinatubo-like eruption using the MAECHAM5-HAM coupled aerosol-climate model with  
203 SO<sub>2</sub> injections of 17 Tg and prescribed climatological sea surface temperatures (Toohey et al., 2011).  
204 Figure 3 shows lower stratospheric zonal mean temperature anomalies (at 100 hPa) and zonal wind  
205 anomalies (at 50 hPa) for these simulations, in comparison with ERA-Interim post-volcanic anomalies  
206 described in Sec. 2.1. Most of the MAECHAM5-HAM ensemble members (roughly 9/12) show  
207 characteristics of a strengthened polar vortex in the lower stratosphere, as quantified as negative  
208 temperature anomalies at polar latitudes and positive zonal wind anomalies between 60° and 80°N in  
209 Fig. 3. However, the ensemble variability of the simulations is pronounced, with 3 members showing a  
210 weakened polar vortex with positive temperature anomalies over the polar cap and negative wind  
211 anomalies between 60° and 80°N. From the full 12-member ensemble, two subsets were defined based  
212 on the zonal wind anomalies, with strong and weak vortex composites (hereafter SVC and WVC)  
213 selected respectively as the 3 members with the most positive and most negative zonal wind anomalies  
214 at 50 hPa and 70°N. Aerosol properties (aerosol extinction at 0.55 μm and effective radius) for these two  
215 composites were collected for use in MPI-ESM simulations. SVC and WVC zonal mean AOD timeseries,  
216 scaled to 1 μm so as to be consistent with the observation-based AOD timeseries, are shown in Fig. 1.

217

#### 218 **2.5 Experiments**

219

220 The forcing sets described above were used to force four sixteen-member ensemble simulations of the  
221 Pinatubo eruption time period. The number of MPI-ESM realizations used here is therefore notably  
222 greater than the three MPI-ESM realizations used in prior single- (Schmidt et al., 2013) or multi-model  
223 (Charlton-Perez et al., 2013; Driscoll et al., 2012) investigations of the CMIP5 historical simulations. Ten  
224 of the sixteen unique initial condition states (at June 1991) were taken from ten independent, pre-  
225 existing CMIP5 historical simulations. In order to increase the ensemble size, six of the historical  
226 simulations were restarted in 1980 with a small atmospheric perturbation applied, and integrated until



227 1991. All simulations were therefore forced with S98 volcanic forcing up until June 1991, at which point  
228 forcing either continued as S98, or switched to one of the other forcings.

229

230 A control ensemble (CTL) is based on the five year period 1986-1990 for the original ten historical  
231 simulations used to produce the initial conditions, comprising in total 50 years, during which the other  
232 external forcings are negligibly different from 1991-1992 conditions. Anomalies for the volcanic  
233 ensembles are computed by differencing ensemble mean results with the CTL ensemble mean.

234

235 Observations imply that the NH winter vortex response to volcanic forcing may last for two years. While  
236 considering the results for the first two winters together certainly increases the ensemble size, it is quite  
237 possible that the mechanisms leading to vortex response are different in the first and second winters  
238 after an eruption. The magnitude of aerosol forcing will be different for the two winters for any forcing  
239 set, with typically stronger aerosol forcing occurring in the first winter. Such temporal changes are likely  
240 larger than differences between the different forcing sets used in this study. With these potential  
241 complications in mind, in order to simplify the analysis and interpretation of the model results in this  
242 study, we choose to focus our analysis only on the first winter after the Pinatubo eruption.

243

244 Unless stated, results shown are ensemble means. Confidence intervals (95% level) are calculated for  
245 differences between forced and CTL ensemble means and the differences between the forced ensemble  
246 means using a bootstrapping technique, with 1000 resamples of the original ensembles. For example,  
247 for each latitude and pressure level, and for each forced ensemble, 1000 bootstrapped sample means  
248 are produced by sampling the 16 ensemble member values with replacement, resulting in an  
249 approximation of the uncertainty distribution for the mean value. The same process is applied to the CTL  
250 ensemble, with  $n=50$ . The difference between the two bootstrapped distributions defines the  
251 uncertainty in the mean difference, and is used to define the 95% confidence interval of the ensemble  
252 mean difference. A parallel procedure is used to define the confidence intervals for the differences of  
253 two volcanically forced ensembles.

254

## 255 **3 Results**

256

### 257 **3.1 Radiative forcing**

258

259 Latitude-pressure plots of zonal mean DJF 1  $\mu\text{m}$  extinction (EXT) are shown in Fig. 4 for the S98 and  
260 SAGE\_4 $\lambda$  forcing sets. A major difference between the two forcing sets is the vertical distribution of  
261 extinction in the tropics, with SAGE\_4 $\lambda$  extinction being more constrained to the lower stratosphere,  
262 compared to S98 which has considerable extinction extending down into the upper troposphere. This  
263 difference in tropical extinction is the result of improvements in the SAGE\_4 $\lambda$  retrieval: the S98 vertical  
264 distribution in the tropics is very likely unrealistic (Arfeuille et al., 2013). The two forcing sets also differ  
265 in terms of the magnitude of tropical extinction, with SAGE\_4 $\lambda$  having stronger extinction in the tropical  
266 lower stratosphere for all wavelengths greater than 0.55  $\mu\text{m}$ . Differences in extinction magnitude are  
267 also apparent in the high latitude lower stratosphere of both hemispheres, with SAGE\_4 $\lambda$  extinction  
268 much smaller than that of S98.

269

270 Direct aerosol radiative heating rates ( $Q^{\text{aer}}$ ) are computed by performing radiative transfer calculations  
271 at each model timestep twice, once with and once without the volcanic aerosols [as in *Stenchikov et al.*,  
272 1998]. We have calculated  $Q^{\text{aer}}$  for single realizations of each forced ensemble.

273

274 Net (longwave + shortwave)  $Q^{\text{aer}}$  for DJF for the two observation-based forcing sets is shown in Figure 4.  
275  $Q^{\text{aer}}$  values are positive over most of the stratosphere for both S98 and SAGE\_4 $\lambda$  forcings, with highest  
276 magnitude in the tropical lower stratosphere at approximately 30 hPa, just north of the equator. Like  
277 the extinction values (Fig. 4, upper row), S98 heating rates are spread over a larger vertical extent than  
278 SAGE\_4 $\lambda$  heating rates: at the equator, S98 heating rates  $> 0.1$  K/day extend from  $\sim 100$  hPa upwards  
279 whereas for the SAGE\_4 $\lambda$  forcing set, heating rates  $> 0.1$  K/day begin  $\sim 60$  hPa. Like the extinction at 1  $\mu\text{m}$   
280 (and longer wavelengths) SAGE\_4 $\lambda$  forcing leads to stronger  $Q^{\text{aer}}$ , with maximum values of 0.5 K/day  
281 compared to max values of 0.3 K/day for S98. Although minor compared to the differences in the  
282 tropical stratosphere, there are differences in  $Q^{\text{aer}}$  in the NH polar latitudes, with S98 leading to slightly  
283 larger  $Q^{\text{aer}}$  values in the NH polar lower stratosphere than for SAGE\_4 $\lambda$ .

284

285 Figure 5 shows DJF 1  $\mu\text{m}$  aerosol extinction for the SVC and WVC forcing sets. Compared to the  
286 observation-based forcing sets, both model-based forcing sets have greater magnitudes of aerosol  
287 extinction, especially in the high latitudes. Such differences likely arise from a combination of (1)  
288 underestimates in the observation-based forcing sets due to saturation effects, especially in the weeks  
289 directly following the eruption, and (2) potential errors in the model simulations, either in terms of  
290 general model deficiencies, or errors in the model formulation in regards to the actual Pinatubo

291 eruption (e.g., SO<sub>2</sub> injection amount or height). The model-based extinctions also have stronger  
292 gradients (both vertical and horizontal) across the tropopause compared to the observation-based  
293 forcing sets. These differences, especially in the vertical, are likely due to the limited vertical resolution  
294 of the observations. The primary difference between the SVC and WVC forcings is the hemispheric  
295 partitioning of the aerosol extinction, with WVC having larger extinctions in the NH than SVC. We  
296 interpret this difference as a result of wave driven circulation in the NH: in cases of strong NH wave  
297 forcing in the original MAECHAM5-HAM runs, a stronger residual circulation transports more aerosol  
298 from the tropical region towards the NH, while also disturbing the NH polar vortex. Therefore, by  
299 selecting cases of weak polar vortex, we also select cases of strong northward aerosol transport.  
300 Another major difference is the magnitude of extinction in the NH high latitudes, and therefore the  
301 gradient in extinction around 60°N. The stronger aerosol extinction gradient in the SVC forcing set is  
302 obviously a result of the strong vortex in the MAECHAM5-HAM simulations, which inhibits mixing of  
303 aerosol into the polar cap. In the tropics, SVC and WVC have very small differences, and their vertical  
304 distribution is almost identical.

305

306  $Q^{\text{aer}}$  values from the model-based forcing sets, also shown in Fig. 5, are more similar to the observation-  
307 based  $Q^{\text{aer}}$  values than the extinctions: the differences in high latitude extinction have relatively little  
308 impact on the  $Q^{\text{aer}}$  differences due to the much weaker LW radiation field here than in the tropics.  
309 Differences in  $Q^{\text{aer}}$  between the two model-based forcing ensembles are relatively small (compared to  
310 differences between the two observation-based forcing ensembles), and are characterized primarily by  
311 the north-south shift between the two forcing sets, and the gradients in  $Q^{\text{aer}}$  at 60°S and 60°N. At high  
312 latitudes,  $Q^{\text{aer}}$  values are apparently not strongly dependent on the aerosol extinction, e.g., SVC has  
313 smaller aerosol extinction values in polar latitudes than WVC, but shows larger  $Q^{\text{aer}}$ . This is likely due to  
314 the fact that the net (absorption-emission) long wave heating rate is strongly temperature dependent  
315 because of the temperature dependence of the emission. As shown below, the SVC ensemble is  
316 characterized by a colder polar vortex than for WVC, which should lead to less emission and thus larger  
317 net heating.

318

### 319 **3.2 Temperature and zonal wind response**

320

321 In order to determine which thermal and dynamical responses to the volcanic forcings are robust across  
322 the different forcings, results are first examined by concatenating the 64 volcanic simulations into one

323 “grand” ensemble (VOLC), with ensemble mean anomalies of temperature and zonal wind shown in Fig.  
324 6.

325  
326 Significant and robust temperature responses in the volcanic simulations include positive anomalies in  
327 the tropical lower stratosphere and negative temperature anomalies in the troposphere, extending to  
328 the surface between approximately 70°S-45°N. In the NH high latitude stratosphere, the temperature  
329 anomaly structure for the VOLC ensemble is roughly consistent with that shown by Schmidt et al. (2013)  
330 for three MPI-ESM realizations (using S98 forcing), with positive temperature anomalies in the upper  
331 stratosphere and mesosphere. However, while temperature anomalies for the VOLC ensemble are  
332 significant throughout most of the tropopause and lower-to-middle stratosphere, anomalies in the NH  
333 polar region are generally not significant.

334  
335 Significant zonal wind responses in the VOLC ensemble include weakening of the subtropical jets at ~30°  
336 and ~100hPa of both hemispheres by 2-4 m/s, and a weakening of the SH stratospheric easterlies by 4-6  
337 m/s. Grand ensemble mean zonal wind anomalies in the NH high latitude stratosphere reach a  
338 maximum of ~2 m/s, and are not significant.

339  
340 Temperature and zonal wind anomalies are shown separately for the observation- and model-based  
341 forcing ensembles in Figures 7 and 8, respectively. For the observation based forcings S98 and SAGE\_4λ  
342 (Fig. 7), the general features are consistent with the VOLC grand ensemble. In agreement with Q<sup>aer</sup> of  
343 Fig. 4, SAGE\_4λ tropical temperature anomalies are greater in magnitude, with peak values of 4.8 K  
344 compared to 3.6 K for S98. Temperature anomalies are also shifted in height between the two  
345 ensembles, with peak temperature anomalies located at 30 hPa for SAGE\_4λ, compared to 50 hPa for  
346 S98. Differences in tropical temperature anomalies between the two ensembles (right-most column of  
347 Fig. 7) are significant at the 95% confidence level between approximately 200 and 20 hPa. The SAGE\_4λ  
348 ensemble shows slightly larger warming in the polar upper stratosphere, although the difference  
349 between S98 and SAGE\_4λ is not significant.

350  
351 In the NH high latitudes, the S98 ensemble shows a weak (2-3 m/s) increase in westerly wind, while the  
352 SAGE\_4λ ensemble shows a weak (3-4 m/s) negative wind anomaly in the upper  
353 stratosphere/mesosphere. Differences between the two ensembles are not significant in the mid-to-  
354 high latitudes.

355

356 For the model-based forcing ensembles SVC and WVC, temperature anomalies in the tropics and  
357 midlatitudes are quite similar in structure between the two ensembles and similar to the grand  
358 ensemble mean. In the NH high latitudes, however, the temperature responses are quite different in  
359 structure between the SVC and WVC ensembles. The SVC ensemble produces a NH high latitude  
360 temperature anomaly pattern with significant warming in the upper stratosphere and lower  
361 mesosphere. WVC, on the other hand, gives a temperature anomaly pattern with insignificant positive  
362 temperature anomalies in the polar lower and middle stratosphere. Differences between the two  
363 forcing sets are significant in the polar lower and upper stratosphere.

364

365 Zonal wind anomalies for the model-based forcing ensembles follow from the temperature anomalies.  
366 The SVC ensemble produces a significant strengthening of the NH polar vortex, with peak zonal wind  
367 anomalies 6-8 m/s. The WVC ensemble produces no significant change in NH vortex winds. The  
368 difference between the vortex response in the SVC and WVC ensembles is significant in the polar lower  
369 stratosphere, and in the mid-to-upper stratosphere at the highest latitudes (70-90°N).

370

371 DJF zonal mean zonal wind at 60°N and 10 hPa for each realization of each ensemble is shown in Figure  
372 9. Ensemble means with 95% confidence intervals are also shown. The mean of the control ensemble is  
373 marked by a horizontal dashed line. Consistent with results discussed above, only the SVC ensemble  
374 shows a significant zonal wind response to volcanic forcing, with an ensemble mean 95% interval which  
375 excludes the control mean. In terms of individual ensemble members, 13/16 members of the SVC  
376 ensemble have zonal mean wind greater than the control mean, although clearly all of the members lie  
377 within the natural variability of the control ensemble. Three SVC members have zonal winds weaker  
378 than the control; as such, the response to SVC forcing is not totally robust and the increase in ensemble  
379 mean vortex strength appears to represent a change in the probability of weak vs. strong vortex states.  
380 The WVC and S98 ensembles show ensemble means and spreads very similar to the control ensemble,  
381 with S98 showing a weak and insignificant positive anomaly in wind strength. The SAGE\_4λ ensemble  
382 shows an ensemble mean equal to that of the control ensemble, but interestingly shows some evidence  
383 of a decrease in ensemble variability.

384

### 385 **3.3 Wave-driven circulation response**

386

387 For all ensembles, we have computed transformed Eulerian mean (TEM) diagnostics (Andrews et al.,  
388 1987), including Eliassen-Palm (EP) fluxes, the meridional residual mass circulation stream function ( $\psi^*$ ),  
389 the residual vertical velocity ( $\bar{w}^*$ ), and temperature tendencies due to vertical residual advection.  
390 Ensemble means of these quantities have been compared to values from the control ensemble in order  
391 to compute post-volcanic anomalies in the first NH winter. As for the temperature and zonal wind  
392 anomalies, selected TEM quantities are examined first in terms of the grand VOLC ensemble in Figure  
393 10.

394

395 It is well known that the variability of polar vortex strength is largely controlled by planetary wave drag,  
396 and therefore on the upward wave flux from the troposphere into the stratosphere (Newman et al.,  
397 2001; Polvani and Waugh, 2004). The vertical component of EP-flux ( $F_z$ ) is a commonly used proxy for  
398 the amount of wave activity entering and propagating through the stratosphere. Figure 10 shows DJF  $F_z$   
399 for the control ensemble and anomalies for VOLC volcanic ensemble. Around the tropopause ( $\sim 100$ - $200$   
400 hPa),  $F_z$  anomalies in the VOLC ensemble are negative in the midlatitude ( $30$ - $45^\circ$ ) regions of both  
401 hemispheres, and generally positive in the mid-to-high latitudes ( $45$ - $90^\circ\text{N}$ ). Positive  $F_z$  anomalies are  
402 significant throughout the SH stratosphere, while in the NH, significant positive  $F_z$  anomalies occur  
403 around  $60^\circ\text{N}$  and  $100$  hPa, and extend upwards slanting equatorward with height.

404

405 Convergence of EP-flux (or negative values of EP-flux divergence, EPFD) leads to wave drag, a slowing of  
406 the wintertime westerly (eastward) zonal wind and a poleward residual circulation. Enhanced wave drag  
407 in volcanic simulations is found throughout the SH stratosphere and in the midlatitude NH middle  
408 stratosphere (around  $30^\circ\text{N}$ ,  $10$  hPa, Fig. 10d). Wave drag in the latter location is especially important for  
409 forcing the residual circulation (Shepherd and McLandress, 2011). Figure 10 (e,f) shows the CTL and  
410 VOLC anomalies of the meridional residual circulation stream function. The poleward NH residual  
411 circulation stream function is found to be enhanced in the VOLC ensemble.

412

413 The volcanically-induced residual circulation anomalies drive adiabatic heating anomalies where vertical  
414 motions are induced. Temperature tendency anomalies due to residual vertical velocity (hereafter  $dT_{\bar{w}^*}$ ,  
415 Fig. 10g,h) show clearly the tropical cooling associated with anomalous vertical upwelling, and heating at  
416 the mid and high latitudes due to anomalous downwelling.

417

418 The terms  $dT_{w*}$  and  $Q^{aer}$  are found to dominate the temperature tendency budget compared to other  
419 terms in the TEM diagnostics. Therefore, the temperature anomalies found in the volcanic simulations  
420 can be understood to be primarily the result of the direct (diabatic) aerosol heating  $Q^{aer}$ , and the  
421 indirect, dynamical (adiabatic) heating  $dT_{w*}$ . These terms, along with the corresponding temperature  
422 anomalies, are shown for each of the volcanic ensembles as lower stratosphere (100-20hPa) averages in  
423 Figure 11.

424  
425 Ensemble mean temperature anomalies show roughly similar behavior in the tropics and midlatitudes  
426 (0-55°N) for all ensembles. In the NH polar latitudes, weak positive temperature anomalies are  
427 simulated for the S98, SAGE\_4λ and WVC ensembles, and negative anomalies for the SVC ensemble.  $Q^{aer}$   
428 peaks in the tropics and decays to zero between 30 and 60°N.  $dT_{w*}$  is negative in the tropics, opposing  
429 the  $Q^{aer}$  heating, and becomes generally positive in the extratropics where downward advection occurs.  
430 In the high latitudes,  $dT_{w*}$  is positive for S98, SAGE\_4λ and WVC, but negative for SVC, consistent with the  
431 temperature anomalies (Fig 8). It is thus clear that the differences in temperature anomalies at high  
432 latitudes, and therefore the temperature gradients around 60°N, result from differences in  $dT_{w*}$   
433 between the ensembles. The effect of differences in temperature tendencies on temperature anomalies  
434 is likely amplified at higher latitudes since radiative damping timescales increase with latitude in the  
435 lower stratosphere (Newman and Rosenfield, 1997). These results underscore the point that  
436 temperature gradients at the high latitudes are controlled by the structure of the volcanically induced  
437 residual circulation anomalies rather than the direct aerosol heating.

438  
439 Differences in the dynamical responses to the SVC and WVC volcanic forcings are further explored by  
440 examining TEM diagnostics for these ensembles. As in the VOLC grand ensemble, both model-based  
441 forced ensembles show positive  $F_z$  anomalies throughout the SH stratosphere and negative anomalies in  
442 the subtropical tropopause region (Fig. 12a,b). Positive  $F_z$  anomalies are found at the NH high latitude  
443 lower stratosphere, extending upwards and slanting equatorward with height. However, these positive  
444  $F_z$  anomalies are much stronger (and significant only) in the WVC ensemble.

445  
446 As in the VOLC ensemble, negative EP-flux divergence (wave drag) is significantly enhanced in the SH  
447 stratosphere and in the NH midlatitude middle stratosphere in both the SVC and WVC ensembles (Fig.  
448 10d,e). NH wave EP-flux divergence anomalies are notably stronger in the WVC ensemble between 10  
449 and 100 hPa and 30-60°N; differences between the two ensembles are significant around 100hPa and

450 60°N. Residual circulation anomalies (Fig. 12g,h) show significant poleward circulation cells in both  
451 hemispheres. Notable differences in the form of the induced residual circulation cells between the two  
452 ensembles exist in the lower and middle NH stratosphere, with circulation cells confined to 0-45°N in the  
453 SVC ensemble, and extending 0-90°N in the WVC ensemble. These differences are significant in around  
454 100 hPa and 60°N, and as such appear related to the differences in EP-flux divergence discussed above.  
455 Temperature tendency anomalies due to residual vertical velocity ( $dT_{w*}$ , Fig. 10j,k) show that the broad  
456 residual circulation anomaly cell in the WVC ensemble leads to dynamical heating of the lower  
457 stratosphere extending from ~45N-90°N, while the narrower poleward cell in SVC leads to significant  
458 heating only in the midlatitude (45-60°N) lower stratosphere. Differences in dynamical warming are  
459 marginally significant in the polar lower stratosphere, consistent with the differences in EP-flux  
460 divergence and residual circulation.

461  
462 The TEM fields of Fig. 12 thus show that the significant difference in polar vortex zonal wind response to  
463 the SVC and WVC volcanic forcings comes about due to differences in the wave activity propagating  
464 upwards into the stratosphere from the troposphere. This mechanism is further explored in Fig 13 for all  
465 volcanic ensembles. Fig. 13 (left) shows the relationship between polar vortex wind ( $u$  at 10 hPa, 60°N,  
466 hereafter  $u_{\text{vortex}}$ ) and lower stratosphere polar temperature ( $T$  at 50 hPa, 60-90°N average, hereafter  
467  $T_{\text{vortex}}$ ). Individual ensemble members are shown by circular markers, while ensemble mean values are  
468 shown as triangles on the bottom and right-hand axes. The compact linear relationship between  $u_{\text{vortex}}$   
469 and  $T_{\text{vortex}}$  apparent in the control run is shifted in the volcanic simulations: for a given  $T_{\text{vortex}}$ , the  
470 associated  $u_{\text{vortex}}$  is typically ~5 m/s stronger in the volcanic runs than in CTL. The SVC ensemble mean  
471  $T_{\text{vortex}}$  is similar to the CTL ensemble mean, and correspondingly, the SVC  $u_{\text{vortex}}$  is larger than the CTL  
472 ensemble mean by 5-10 m/s. In contrast, the other volcanic ensembles all show increases in  $T_{\text{vortex}}$ , and  
473 correspondingly,  $u_{\text{vortex}}$  for these ensembles is less than that of SVC, and similar to the CTL ensemble  
474 mean value.

475  
476 Polar lower stratosphere temperatures are related to upward EP-flux in the midlatitudes (Newman et  
477 al., 2001; Polvani and Waugh, 2004). In Fig 13b,  $u_{\text{vortex}}$  is plotted vs.  $F_z$  at 100 hPa averaged over 45-75°N  
478 (hereafter  $F_{z,100}$ , a common scalar metric for wave activity entering the extratropical stratosphere). Polar  
479 vortex strength,  $u_{\text{vortex}}$ , is seen to be stronger for any particular  $F_{z,100}$  value in the volcanic runs compared  
480 to the CTL ensemble. For the SVC ensemble,  $F_{z,100}$  is comparable to the CTL value, and the  $u_{\text{vortex}}$  anomaly  
481 is 5-10 m/s. The other ensembles show positive anomalies in  $F_{z,100}$ ; the zonal wind of these volcanic



482 ensembles are thus reduced due to the increased wave activity and hence wave drag. Post-volcanic  
483 anomalies in  $F_{z,100}$  thus exert a negative feedback on the wind anomalies driven by changes in the lower  
484 stratosphere temperature gradient.

485

#### 486 **4. Discussion**

487

488 A major result of the preceding sections is that the temperature structure of the lower stratosphere in  
489 post-volcanic winters in the high latitudes is controlled primarily by induced residual circulation  
490 anomalies. Post volcanic-eruption enhancement of the stratospheric residual circulation (or BDC) have  
491 been suggested based on previous model studies (Pitari and Mancini, 2002; Pitari, 1993). Graf et al.,  
492 (2007) assessed the observational record and found evidence of increased winter stratospheric wave  
493 activity after three eruptions (Agung, El Chichón and Pinatubo). Poberaj et al., (2011) showed that  
494 anomalously strong EP-fluxes occurred in the SH after Pinatubo. Such increases in winter stratospheric  
495 wave activity are likely a result of changes in the wave propagation conditions of the stratosphere  
496 following aerosol radiative heating, allowing more planetary waves to propagate upwards. Similar  
497 arguments explain climate models' predicted increase in future stratospheric residual circulation due to  
498 changes in the atmospheric temperature structure due to climate change (Garcia and Randel, 2008;  
499 McLandress and Shepherd, 2009; Shepherd and McLandress, 2011), which also enhances the meridional  
500 temperature gradient in the lower stratosphere, albeit at lower altitudes.

501

502 The residual circulation anomalies induced by the volcanic forcing in the ensembles strengthen the  
503 climatological residual circulation, although the structure of the anomalies is different than the  
504 climatology. For example, the induced upwelling is centered on the equator whereas the maximum  
505 climatological upwelling is centered in the summer hemisphere, and the induced upwelling is strongest  
506 above the level of maximum aerosol radiative heating, and even negative below. This latter point may  
507 explain why post-Pinatubo anomalies in tropical upwelling are not apparent in observational records,  
508 which are usually displayed as timeseries of upwelling in the lower stratosphere (Seviour et al., 2012).  
509 We have shown that increased wave activity and wave drag in both hemispheres is a robust response to  
510 volcanic aerosol forcing, and therefore a component of the residual circulation anomalies in the  
511 volcanically-forced simulations results from wave drag anomalies. However, given the fact that  
512 maximum anomalous tropical upwelling occurs at and above the location of maximum aerosol radiative  
513 heating in the tropics, it seems possible that there is also a diabatic component to the anomalous

514 residual circulation, forced directly by the aerosol radiative heating, as suggested by previous studies  
515 (e.g., Aquila et al., 2013; Pitari and Mancini, 2002).

516

517 The lack of NH polar vortex response to the Pinatubo forcings used here does not necessarily rule out  
518 the possibility that other forcings could produce significant vortex responses. Most obviously, the  
519 magnitude of the volcanic forcing may be essentially important. Toohey et al. (2011) found a significant  
520 vortex response to a near-super eruption volcanic forcing, which likely produced a much stronger direct  
521 aerosol radiative heating gradient in the mid to high latitudes. Similarly, Bittner et al., (Sensitivity of the  
522 Northern Hemisphere winter stratosphere variability to the strength of volcanic eruptions, submitted  
523 manuscript) find a significant response of the MPI-ESM NH polar vortex to volcanic forcing representing  
524 that of the 1815 eruption of Tambora. It is also important that our simulations do not include possible  
525 chemical depletion of stratospheric ozone brought about by the presence of volcanic aerosols, or ozone  
526 anomalies due to changes in the residual circulation. Induced changes in the meridional structure of  
527 stratospheric ozone can also affect temperature gradients in the lower stratosphere (Muthers et al.,  
528 2014), and may be a significant feedback in the response of the polar vortex to volcanic forcing.

529

530 While neither of the two observation-based volcanic forcing sets used here produced significant vortex  
531 responses, the difference in the responses was found to be significant at the 95% level. While the  
532 SAGE\_4 $\lambda$  is almost certainly a more accurate reconstruction of the true aerosol evolution than S98 in  
533 many aspects, e.g. the vertical distribution of aerosol extinction in the tropics, it does not produce the  
534 expected increase in NH polar vortex strength in simulations with the MPI-ESM. It actually leads to a  
535 significantly weaker vortex than the S98 forcing, which is especially surprising given it produces stronger  
536 radiative heating in the tropical lower stratosphere than S98.

537

538 While the difference between responses to SVC and WVC forcing was not significant, the SVC was the  
539 only forcing to produce a significant vortex strengthening. Such differences in simulated vortex response  
540 between the different ensembles imply sensitivity in vortex response to the exact structure of the  
541 volcanic forcing. These differences between the ensembles, and especially the significant response of  
542 SVC ensemble should perhaps be taken with a grain of salt: the large variability of wave drag and vortex  
543 dynamics necessitates the use of large ensembles in order to negate the impact of variability on the  
544 ensemble means. While our ensemble size of 16 is larger than most prior single-model volcanic studies,  
545 it may still be insufficient to unambiguously identify significant high latitude responses from volcanic

546 forcing. Furthermore, given the anomalous heating of the lower stratosphere in volcanic simulations, it  
547 could be the case that insignificant anomalies in residual circulation lead to significant anomalies in  
548 ensemble mean temperature gradients and therefore zonal wind. Nevertheless, planetary wave  
549 propagation through the tropopause region has been shown to be quite sensitive to local vertical and  
550 meridional gradients in zonal wind and temperature (e.g., Chen and Robinson, 1992). It is plausible that  
551 small differences in the structure of the prescribed volcanic aerosol forcing, and resulting radiative  
552 heating, temperature and wind, could have relatively large impacts on wave propagation.

553

## 554 **6. Conclusions**

555

556 In simulations of the post-Pinatubo eruption period with the MPI-ESM with four different volcanic  
557 aerosol forcings, an enhanced polar vortex—which is expected based on limited observations and simple  
558 theoretical arguments—was not a robust response. The responses that were significant and robust  
559 across all four forcings in the NH winter stratospheric include: (1) positive temperature anomalies in the  
560 lower tropical stratosphere, (2) enhanced  $F_z$  in the NH midlatitudes (40-60°N) and wave drag in the  
561 midlatitude middle stratosphere, (3) enhanced meridional residual circulation, (4) dynamical cooling of  
562 the tropical lower stratosphere and heating of the midlatitude lower stratosphere.

563

564 The lack of robust polar vortex response to volcanic aerosol forcing in the MPI-ESM simulations of this  
565 work is consistent with the multi-model results of the CMIP5 historical experiments (Charlton-Perez et  
566 al., 2013; Driscoll et al., 2012). We have shown that the meridional temperature gradient in the  
567 extratropical lower stratosphere induced by volcanic aerosol forcing, and therefore the strength of the  
568 induced stratospheric winter polar vortex wind anomalies, is controlled primarily by dynamical heating  
569 associated with the induced residual circulation rather than the direct aerosol radiative heating. The  
570 vortex response in the model is therefore much less robust than would be expected if it were directly  
571 due to the aerosol radiative heating, as it is instead subject to complexity and variability of wave-mean  
572 flow interaction in the winter stratosphere.

573

574 Our results further imply that the NH polar vortex response is quite sensitive to the specific structure of  
575 the volcanic forcing used. Generally, volcanic forcing leads to an overall increase in resolved wave  
576 activity entering the mid- to high latitude stratosphere, and the impact of this wave activity tends to  
577 weaken the polar vortex, counteracting the impact of low-latitude heating. However, one volcanic

578 forcing set used here, the model-based SVC forcing, did not significantly affect high-latitude wave  
579 activity, and thereby produced a strengthened polar vortex, approximately in line with the expected  
580 response. We speculate that such sensitivity is due to the role that minor differences in volcanically  
581 induced temperature and wind anomalies play in wave-mean flow interactions in the stratosphere. An  
582 alternate theory is that differences in volcanic forcing lead to differences in wave generation in the  
583 troposphere. In either case, the results imply that—at least for a Pinatubo magnitude eruption—very  
584 accurate reconstructions of volcanic aerosol forcing would be required to reproduce any impact of the  
585 aerosols on polar vortex strength in climate model simulations.

586

587

#### 588 Acknowledgements

589

590 The authors would like to thank Chao Li and Holger Pohlmann for providing model restart fields from  
591 MPI-ESM simulations. This work was supported by the Federal Ministry for Education and Research in  
592 Germany (BMBF) through the research program “MiKlip” (FKZ:01LP130B(MT):/01LP1130A(CT,MB)).  
593 Computations were done at the German Climate computer center (DKRZ). We acknowledge the  
594 European Centre for Medium-range Weather Forecasts (ECMWF) for our use of ERA-Interim reanalysis  
595 data.

596

#### 597 References

598 Andrews, D. G., Holton, J. R. and Leovy, C. B.: Middle Atmosphere Dynamics, Academic Press., 1987.

599 Aquila, V., Oman, L. D., Stolarski, R., Douglass, A. R. and Newman, P. A.: The Response of Ozone and  
600 Nitrogen Dioxide to the Eruption of Mt. Pinatubo at Southern and Northern Midlatitudes, *J. Atmos. Sci.*,  
601 70(3), 894–900, doi:10.1175/JAS-D-12-0143.1, 2013.

602 Arfeuille, F., Luo, B. P., Heckendorn, P., Weisenstein, D., Sheng, J. X., Rozanov, E., Schraner, M.,  
603 Brönnimann, S., Thomason, L. W. and Peter, T.: Modeling the stratospheric warming following the Mt.  
604 Pinatubo eruption: uncertainties in aerosol extinctions, *Atmos. Chem. Phys.*, 13(22), 11221–11234,  
605 doi:10.5194/acp-13-11221-2013, 2013.

606 Baldwin, M. P. and Dunkerton, T. J.: Stratospheric harbingers of anomalous weather regimes., *Science*,  
607 294(5542), 581–4, doi:10.1126/science.1063315, 2001.

608 Charlton-Perez, A. J., Baldwin, M. P., Birner, T., Black, R. X., Butler, A. H., Calvo, N., Davis, N. A., Gerber,  
609 E. P., Gillett, N., Hardiman, S., Kim, J., Krüger, K., Lee, Y.-Y., Manzini, E., McDaniel, B. A., Polvani, L.,  
610 Reichler, T., Shaw, T. A., Sigmund, M., Son, S.-W., Toohey, M., Wilcox, L., Yoden, S., Christiansen, B., Lott,

- 611 F., Shindell, D., Yukimoto, S. and Watanabe, S.: On the lack of stratospheric dynamical variability in low-  
612 top versions of the CMIP5 models, *J. Geophys. Res. Atmos.*, 118(6), 2494–2505, doi:10.1002/jgrd.50125,  
613 2013.
- 614 Chen, P. and Robinson, W. A.: Propagation of Planetary Waves between the Troposphere and  
615 Stratosphere, *J. Atmos. Sci.*, 49(24), 2533–2545, doi:10.1175/1520-  
616 0469(1992)049<2533:POPWBT>2.0.CO;2, 1992.
- 617 Christiansen, B.: Volcanic Eruptions, Large-Scale Modes in the Northern Hemisphere, and the El Niño–  
618 Southern Oscillation, *J. Clim.*, 21(5), 910, doi:10.1175/2007JCLI1657.1, 2008.
- 619 Crowley, T., Zielinski, G., Vinther, B. M., Udisti, R., Kreutz, K., Cole-Dai, J. and Castellano, E.: Volcanism  
620 and the little ice age, *PAGES Newsl.*, 16(2), 22–23, 2008.
- 621 Dee, D. P., Uppala, S. M., Simmons, A. J., Berrisford, P., Poli, P., Kobayashi, S., Andrae, U., Balmaseda, M.  
622 A., Balsamo, G., Bauer, P., Bechtold, P., Beljaars, A. C. M., van de Berg, L., Bidlot, J., Bormann, N., Delsol,  
623 C., Dragani, R., Fuentes, M., Geer, A. J., Haimberger, L., Healy, S. B., Hersbach, H., Hólm, E. V., Isaksen, L.,  
624 Kållberg, P., Köhler, M., Matricardi, M., McNally, A. P., Monge-Sanz, B. M., Morcrette, J.-J., Park, B.-K.,  
625 Peubey, C., de Rosnay, P., Tavolato, C., Thépaut, J.-N. and Vitart, F.: The ERA-Interim reanalysis:  
626 configuration and performance of the data assimilation system, *Q. J. R. Meteorol. Soc.*, 137(656), 553–  
627 597, doi:10.1002/qj.828, 2011.
- 628 Driscoll, S., Bozzo, A., Gray, L. J., Robock, A. and Stenchikov, G.: Coupled Model Intercomparison Project  
629 5 (CMIP5) simulations of climate following volcanic eruptions, *J. Geophys. Res.*, 117(D17),  
630 doi:10.1029/2012JD017607, 2012.
- 631 Eyring, V. and Lamarque, J.-F.: Overview of IGAC/SPARC Chemistry-Climate Model Initiative (CCMI)  
632 Community Simulations in Support of Upcoming Ozone and Climate Assessments, *SPARC Newsl.*, (No.  
633 40), 48–66, 2013.
- 634 Garcia, R. R. and Randel, W. J.: Acceleration of the Brewer–Dobson Circulation due to Increases in  
635 Greenhouse Gases, *J. Atmos. Sci.*, 65(8), 2731–2739, doi:10.1175/2008JAS2712.1, 2008.
- 636 Gerber, E. P., Butler, A., Calvo, N., Charlton-Perez, A., Giorgetta, M., Manzini, E., Perlwitz, J., Polvani, L.  
637 M., Sassi, F., Scaife, A. A., Shaw, T. A., Son, S.-W. and Watanabe, S.: Assessing and Understanding the  
638 Impact of Stratospheric Dynamics and Variability on the Earth System, *Bull. Am. Meteorol. Soc.*, 93(6),  
639 845–859, doi:10.1175/BAMS-D-11-00145.1, 2012.
- 640 Giorgetta, M. A., Jungclaus, J., Reick, C. H., Legutke, S., Bader, J., Böttinger, M., Brovkin, V., Crueger, T.,  
641 Esch, M., Fieg, K., Glushak, K., Gayler, V., Haak, H., Hollweg, H.-D., Ilyina, T., Kinne, S., Kornblueh, L.,  
642 Matei, D., Mauritsen, T., Mikolajewicz, U., Mueller, W., Notz, D., Pithan, F., Raddatz, T., Rast, S., Redler,  
643 R., Roeckner, E., Schmidt, H., Schnur, R., Segschneider, J., Six, K. D., Stockhause, M., Timmreck, C.,  
644 Wegner, J., Widmann, H., Wieners, K.-H., Claussen, M., Marotzke, J. and Stevens, B.: Climate and carbon  
645 cycle changes from 1850 to 2100 in MPI-ESM simulations for the coupled model intercomparison project  
646 phase 5, *J. Adv. Model. Earth Syst.*, n/a–n/a, doi:10.1002/jame.20038, 2013.

- 647 Graf, H.-F., Kirchner, I., Robock, A. and Schult, I.: Pinatubo eruption winter climate effects: model versus  
648 observations, *Clim. Dyn.*, 9(2), doi:10.1007/BF00210011, 1993.
- 649 Graf, H.-F., Li, Q. and Giorgetta, M. A.: Volcanic effects on climate: revisiting the mechanisms, *Atmos.*  
650 *Chem. Phys.*, 7(17), 4503–4511, doi:10.5194/acp-7-4503-2007, 2007.
- 651 Kirchner, I., Stenchikov, G. L., Graf, H.-F., Robock, A. and Antuña, J. C.: Climate model simulation of  
652 winter warming and summer cooling following the 1991 Mount Pinatubo volcanic eruption, *J. Geophys.*  
653 *Res.*, 104(D16), 19039–19055, doi:10.1029/1999JD900213, 1999.
- 654 Kodera, K.: Influence of volcanic eruptions on the troposphere through stratospheric dynamical  
655 processes in the northern hemisphere winter, *J. Geophys. Res.*, 99(D1), 1273, doi:10.1029/93JD02731,  
656 1994.
- 657 Kodera, K.: On the origin and nature of the interannual variability of the winter stratospheric circulation  
658 in the northern hemisphere, *J. Geophys. Res.*, 100(D7), 14077, doi:10.1029/95JD01172, 1995.
- 659 Labitzke, K. and van Loon, H.: The Southern Oscillation. Part IX: The Influence of Volcanic Eruptions on  
660 the Southern Oscillation in the stratosphere., *J. Clim.*, 2(10), doi:10.1175/1520-  
661 0442(1989)002<1223:TSOPIT>2.0.CO;2, 1989.
- 662 Labitzke, K. and McCormick, M. P.: Stratospheric temperature increases due to Pinatubo aerosols,  
663 *Geophys. Res. Lett.*, 19(2), 207, doi:10.1029/91GL02940, 1992.
- 664 Marshall, A. G., Scaife, A. A. and Ineson, S.: Enhanced Seasonal Prediction of European Winter Warming  
665 following Volcanic Eruptions, *J. Clim.*, 22(23), 6168, doi:10.1175/2009JCLI3145.1, 2009.
- 666 McLandress, C. and Shepherd, T. G.: Simulated Anthropogenic Changes in the Brewer–Dobson  
667 Circulation, Including Its Extension to High Latitudes, *J. Clim.*, 22(6), 1516–1540,  
668 doi:10.1175/2008JCLI2679.1, 2009.
- 669 Muthers, S., Anet, J. G., Raible, C. C., Brönnimann, S., Rozanov, E., Arfeuille, F., Peter, T., Shapiro, a. I.,  
670 Beer, J., Steinhilber, F., Brugnara, Y. and Schmutz, W.: Northern hemispheric winter warming pattern  
671 after tropical volcanic eruptions: Sensitivity to the ozone climatology, *J. Geophys. Res. Atmos.*, n/a–n/a,  
672 doi:10.1002/2013JD020138, 2014.
- 673 Newman, P. A., Nash, E. R. and Rosenfield, J. E.: What controls the temperature of the Arctic  
674 stratosphere during the spring?, *J. Geophys. Res.*, 106(D17), 19999, doi:10.1029/2000JD000061, 2001.
- 675 Newman, P. A. and Rosenfield, J. E.: Stratospheric thermal damping times, *Geophys. Res. Lett.*, 24(4),  
676 433–436, doi:10.1029/96GL03720, 1997.
- 677 Perlwitz, J. and Graf, H.-F.: The Statistical Connection between Tropospheric and Stratospheric  
678 Circulation of the Northern Hemisphere in Winter., *J. Clim.*, 8(10), doi:10.1175/1520-  
679 0442(1995)008<2281:TSCBTA>2.0.CO;2, 1995.

680 Pitari, G.: A numerical study of the possible perturbation of stratospheric dynamics due to Pinatubo  
681 aerosols - Implications for tracer transport, *J. Atmos. Sci.* (ISSN 0022-4928), 50, 2443–2461,  
682 doi:10.1175/1520-0469(1993)050<2443:ANSOTP>2.0.CO;2, 1993.

683 Pitari, G. and Mancini, E.: Short-term climatic impact of the 1991 volcanic eruption of Mt. Pinatubo and  
684 effects on atmospheric tracers, *Nat. Hazards Earth Syst. Sci.*, 2(1), 2002.

685 Poberaj, C. S., Staehelin, J. and Brunner, D.: Missing Stratospheric Ozone Decrease at Southern  
686 Hemisphere Middle Latitudes after Mt. Pinatubo: A Dynamical Perspective, *J. Atmos. Sci.*, 68(9), 1922–  
687 1945, doi:10.1175/JAS-D-10-05004.1, 2011.

688 Polvani, L. M. and Waugh, D. W.: Upward Wave Activity Flux as a Precursor to Extreme Stratospheric  
689 Events and Subsequent Anomalous Surface Weather Regimes., *J. Clim.*, 17(18), doi:10.1175/1520-  
690 0442(2004)017<3548:UWAFAA>2.0.CO;2, 2004.

691 Robock, A.: Volcanic Eruptions and Climate, *Rev. Geophys.*, 38(2), 191–219, doi:10.1029/1998RG000054,  
692 2000.

693 Robock, A. and Mao, J.: Winter warming from large volcanic eruptions, *Geophys. Res. Lett.*, 19(24), 2405,  
694 doi:10.1029/92GL02627, 1992.

695 Rozanov, E. V.: Climate/chemistry effects of the Pinatubo volcanic eruption simulated by the UIUC  
696 stratosphere/troposphere GCM with interactive photochemistry, *J. Geophys. Res.*, 107(D21), 4594,  
697 doi:10.1029/2001JD000974, 2002.

698 Russell, P. B., Livingston, J. M., Pueschel, R. F., Bauman, J. J., Pollack, J. B., Brooks, S. L., Hamill, P.,  
699 Thomason, L. W., Stowe, L. L., Deshler, T., Dutton, E. G. and Bergstrom, R. W.: Global to microscale  
700 evolution of the Pinatubo volcanic aerosol derived from diverse measurements and analyses, *J.*  
701 *Geophys. Res.*, 101(D13), 18745–18763, doi:10.1029/96JD01162, 1996.

702 Sato, M., Hansen, J. E., McCormick, M. P. and Pollack, J. B.: Stratospheric Aerosol Optical Depths, 1850–  
703 1990, *J. Geophys. Res.*, 98(D12), 22987–22994, doi:10.1029/93JD02553, 1993.

704 Schmidt, H., Rast, S., Bunzel, F., Esch, M., Giorgetta, M., Kinne, S., Krismer, T., Stenchikov, G., Timmreck,  
705 C., Tomassini, L. and Walz, M.: Response of the middle atmosphere to anthropogenic and natural  
706 forcings in the CMIP5 simulations with the Max Planck Institute Earth system model, *J. Adv. Model.*  
707 *Earth Syst.*, n/a–n/a, doi:10.1002/jame.20014, 2013.

708 Seviour, W. J. M., Butchart, N. and Hardiman, S. C.: The Brewer–Dobson circulation inferred from ERA–  
709 Interim, *Q. J. R. Meteorol. Soc.*, 138(665), 878–888, doi:10.1002/qj.966, 2012.

710 Shepherd, T. G. and McLandress, C.: A Robust Mechanism for Strengthening of the Brewer–Dobson  
711 Circulation in Response to Climate Change: Critical-Layer Control of Subtropical Wave Breaking, *J.*  
712 *Atmos. Sci.*, 68(4), 784–797, doi:10.1175/2010JAS3608.1, 2011.

713 Shindell, D. T.: Dynamic winter climate response to large tropical volcanic eruptions since 1600, *J.*  
714 *Geophys. Res.*, 109(D5), doi:10.1029/2003JD004151, 2004.

715 Shindell, D. T., Schmidt, G. A., Miller, R. L. and Rind, D.: Northern hemisphere winter climate response to  
716 greenhouse gas, ozone, solar, and volcanic forcing, *J. Geophys. Res.*, 106(D7), 7193,  
717 doi:10.1029/2000JD900547, 2001.

718 Stenchikov, G.: Arctic Oscillation response to the 1991 Mount Pinatubo eruption: Effects of volcanic  
719 aerosols and ozone depletion, *J. Geophys. Res.*, 107(D24), doi:10.1029/2002JD002090, 2002.

720 Stenchikov, G., Hamilton, K., Stouffer, R. J., Robock, A., Ramaswamy, V., Santer, B. and Graf, H.-F.: Arctic  
721 Oscillation response to volcanic eruptions in the IPCC AR4 climate models, *J. Geophys. Res.*, 111(D7),  
722 doi:10.1029/2005JD006286, 2006.

723 Stenchikov, G. L., Kirchner, I., Robock, A., Graf, H.-F., Antuña, J. C., Grainger, R. G., Lambert, A. and  
724 Thomason, L.: Radiative forcing from the 1991 Mount Pinatubo volcanic eruption, *J. Geophys. Res.*,  
725 103(D12), 13837–13857, doi:10.1029/98JD00693, 1998.

726 Thomason, L. W. and Peter, T., Eds.: Assessment of Stratospheric Aerosol Properties (ASAP), SPARC  
727 Report No. 4, WCRP- 124, WMO/TD-No. 1295., 2006.

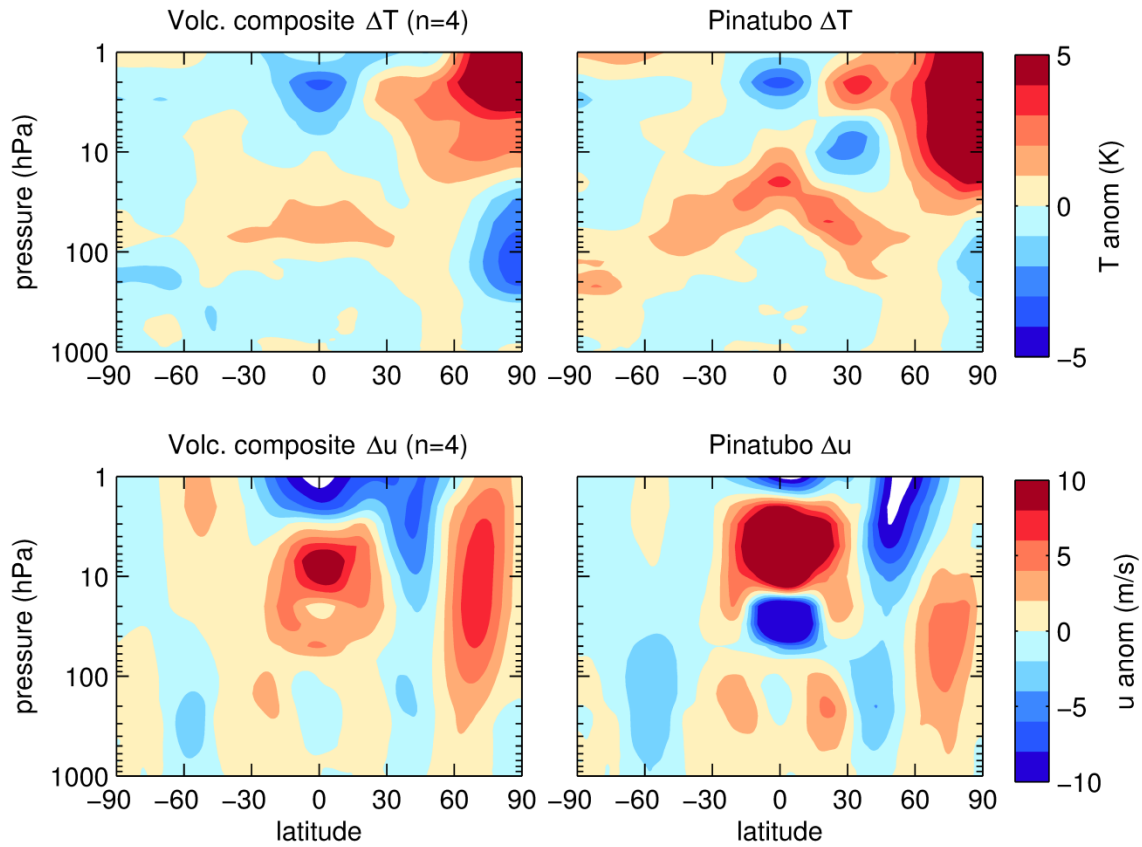
728 Timmreck, C., Graf, H.-F., Lorenz, S. J., Niemeier, U., Zanchettin, D., Matei, D., Jungclaus, J. H. and  
729 Crowley, T. J.: Aerosol size confines climate response to volcanic super-eruptions, *Geophys. Res. Lett.*,  
730 37(24), L24705, doi:10.1029/2010GL045464, 2010.

731 Timmreck, C., Lorenz, S. J., Crowley, T. J., Kinne, S., Raddatz, T. J., Thomas, M. A. and Jungclaus, J. H.:  
732 Limited temperature response to the very large AD 1258 volcanic eruption, *Geophys. Res. Lett.*, 36(21),  
733 doi:10.1029/2009GL040083, 2009.

734 Toohey, M., Krüger, K., Niemeier, U. and Timmreck, C.: The influence of eruption season on the global  
735 aerosol evolution and radiative impact of tropical volcanic eruptions, *Atmos. Chem. Phys.*, 11(23),  
736 12351–12367, doi:10.5194/acp-11-12351-2011, 2011.

737

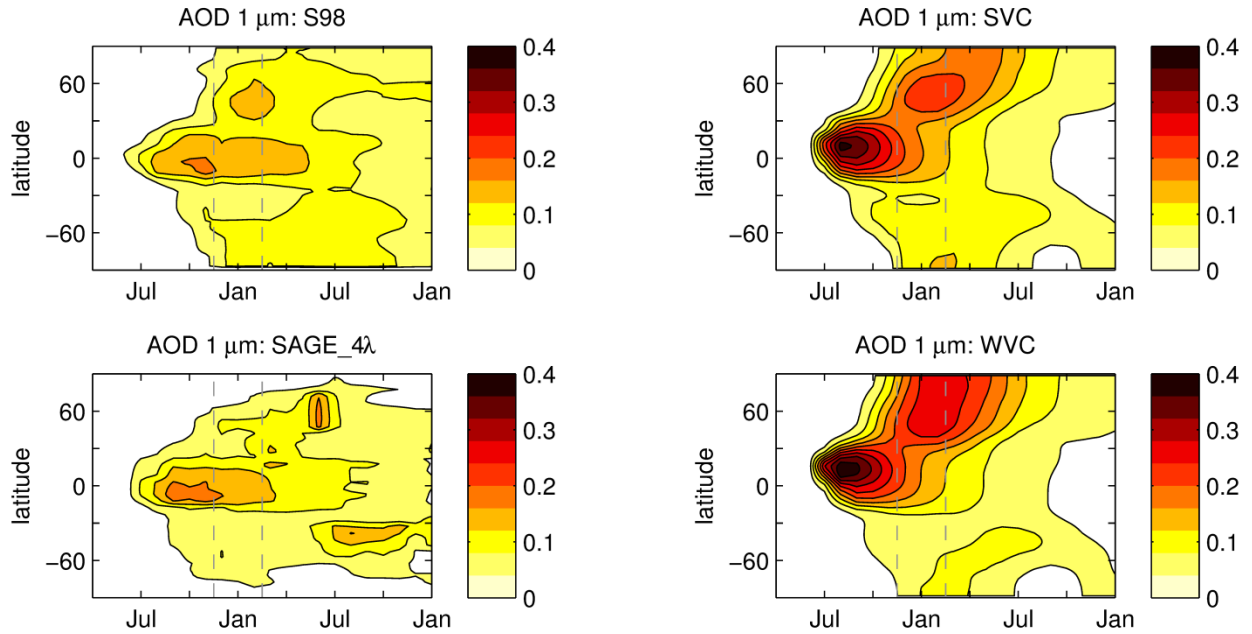




738

739 Figure 1: ERA-Interim DJF (top) temperature and (bottom) zonal wind anomalies for (left) post-volcanic  
 740 composite ( $n=4$ ) of two winters after eruptions of El Chichón and Pinatubo, and (right) 1991/92, the first  
 741 winter after the Pinatubo eruption.

742

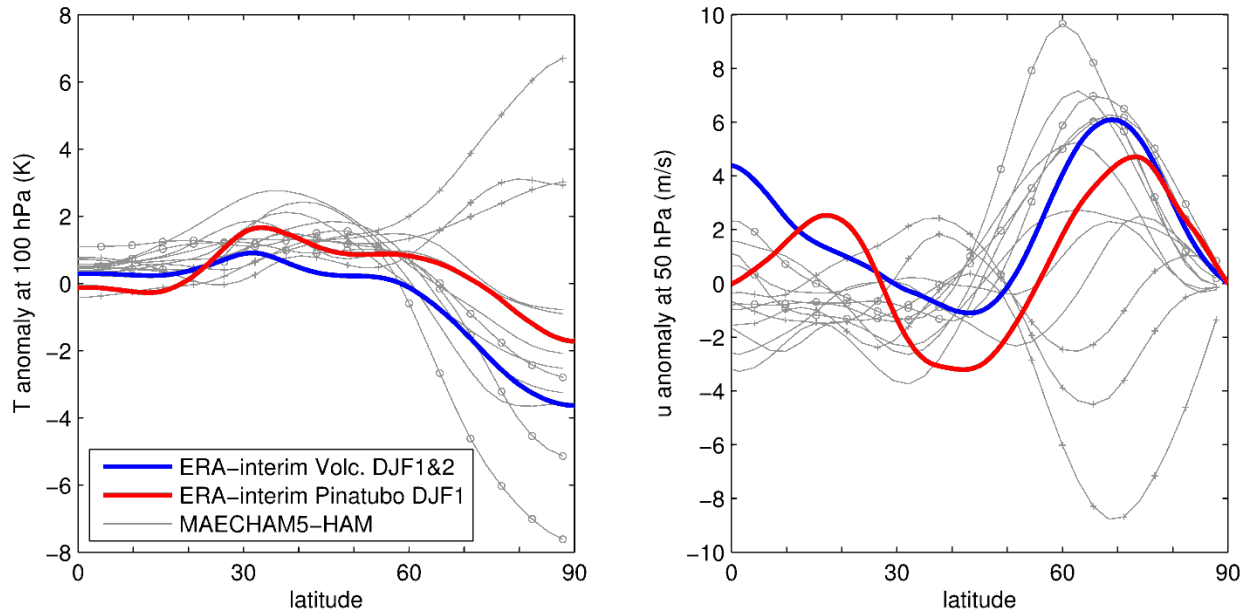


743

744

745 Figure 2: Zonal mean aerosol optical depth at 1  $\mu\text{m}$  timeseries for the Pinatubo eruption, as  
 746 reconstructed from observations producing the S98 and SAGE\_4 $\lambda$  forcing datasets (left) and based on  
 747 MAECHAM5-HAM model simulations (right) and composited according to strong (SVC) and weak (WVC)  
 748 vortex states. Gray vertical lines demark the DJF period of interest.

749



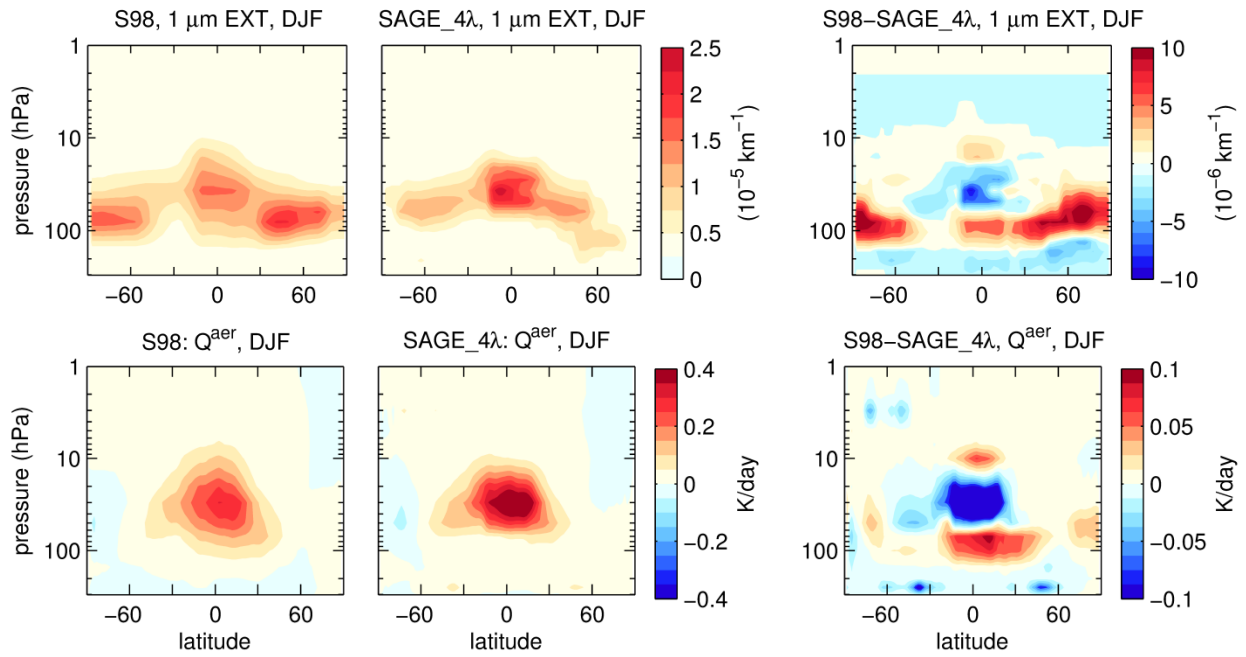
750

751 Figure 3: First post-eruption NH winter (DJF) anomalies of (left) temperature at 100 hPa and (right) zonal  
 752 wind at 50 hPa for the 12 member MAECHAM5-HAM Pinatubo ensemble of (Toohey et al., 2011)(gray  
 753 lines). Ensemble members comprising the strong and weak vortex composites (SVC and WVC) as defined  
 754 in the main text are marked by circle and cross markers, respectively. For comparison, ERA-Interim  
 755 anomalies based on a composite of the 2 winters after the eruptions of El Chichón and Pinatubo (blue),  
 756 and the single winter after the Pinatubo eruption (red) are also shown.

757

758

759

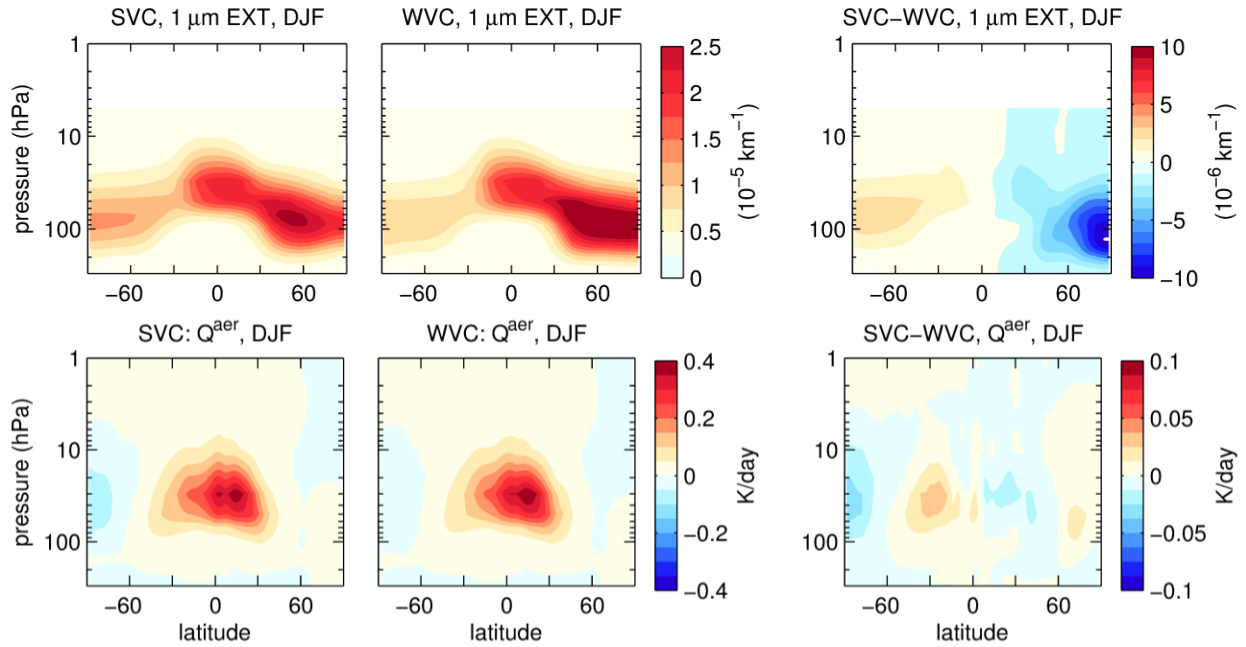


760

761 Figure 4: (top) latitude-pressure distributions of 1  $\mu\text{m}$  aerosol extinction in the S98 and SAGE\_4 $\lambda$   
762 volcanic aerosol forcing sets in first DJF after Pinatubo (winter 1991/92). (bottom) aerosol radiative  
763 heating ( $Q^{\text{aer}}$ ) as computed within the MPI-ESM model for each forcing set. Right-hand column shows  
764 S98-SAGE\_4 $\lambda$  differences for both 1  $\mu\text{m}$  extinction and  $Q^{\text{aer}}$ .

765

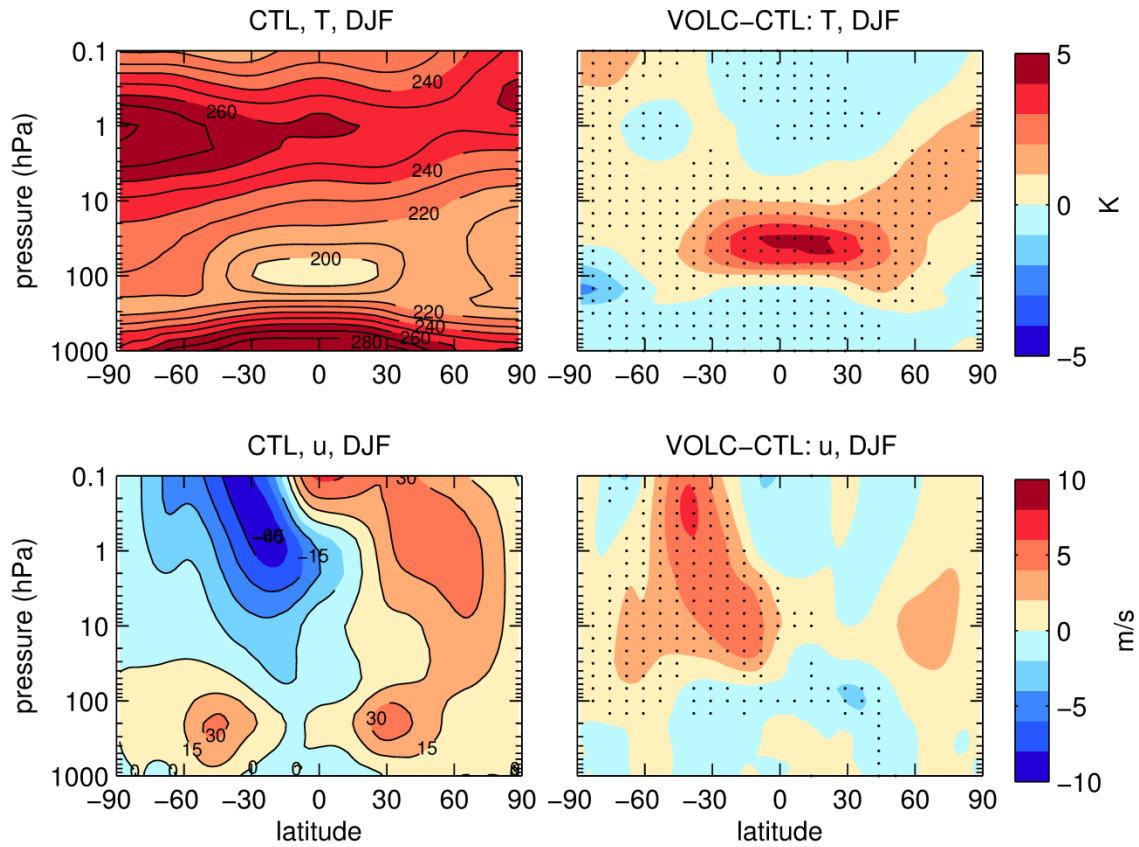
766



767

768 Figure 5: (top) latitude-pressure distributions of 1 μm aerosol extinction in the SVC and WVC volcanic  
769 aerosol forcing sets in first DJF after Pinatubo (winter 1991/92). (bottom) aerosol radiative heating (Q<sup>aer</sup>)  
770 as computed within the MPI-ESM model for each forcing set. Right-hand column shows SVC-WVC  
771 differences for both 1 μm extinction and Q<sup>aer</sup>.

772



773

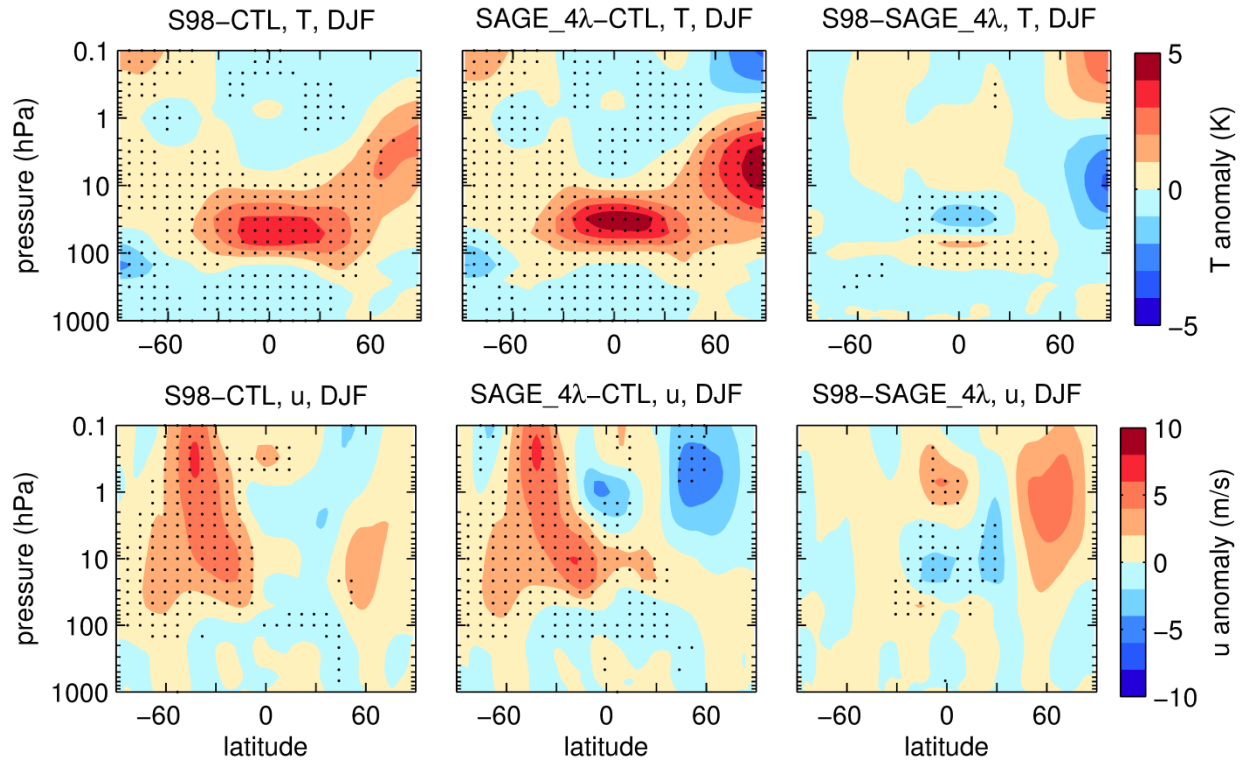
774 Figure 6: DJF temperature (top) and zonal wind (bottom) from the CTL ensemble (left) and anomalies for  
 775 the VOLC grand ensemble (right). Hatching highlights anomalies which are significant at the 95%  
 776 confidence level based on a bootstrapping algorithm.

777

778

779

780

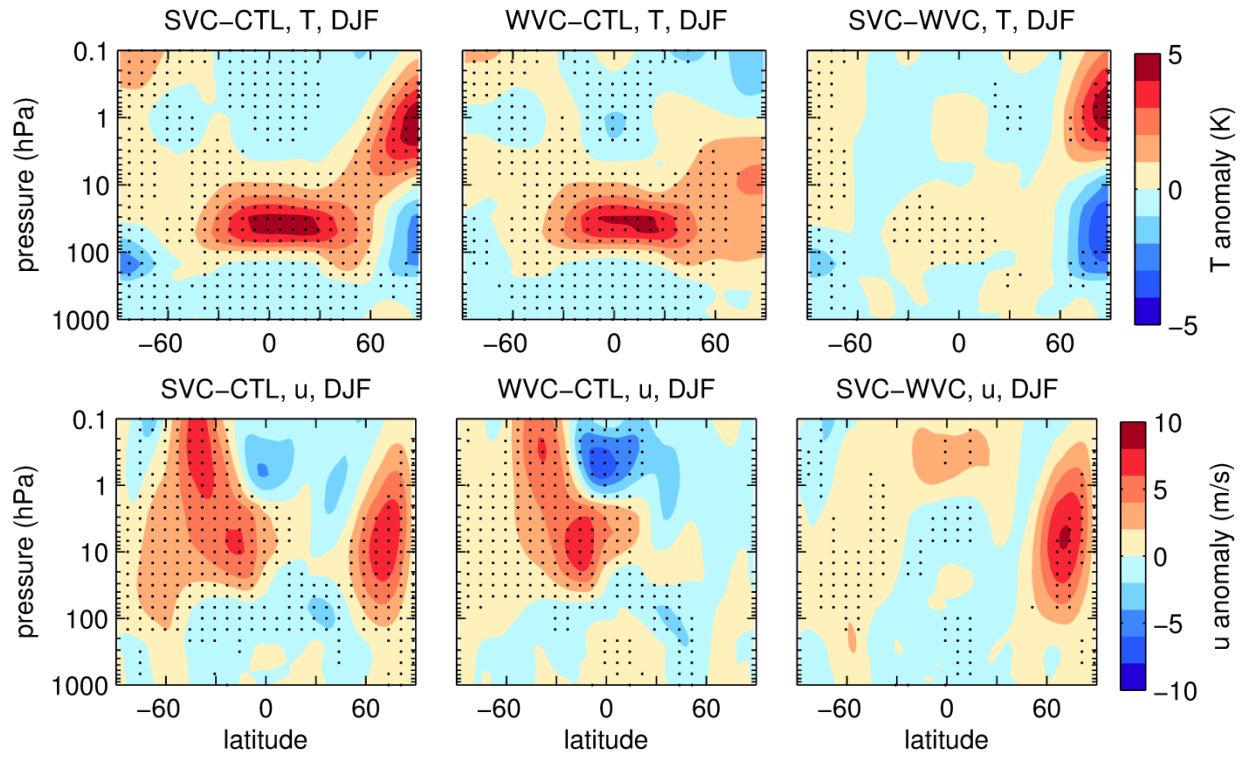


781

782

783 Figure 7: Temperature and zonal wind response of the observations-based volcanic forced ensembles.  
 784 Shown are DJF anomalies for the (left) S98 and (middle) SAGE\_4λ ensembles, and (right) the difference  
 785 between the two ensembles for (top) temperature and (bottom) zonal wind. Hatching highlights  
 786 anomalies which are significant at the 95% confidence level based on a bootstrapping algorithm.

787



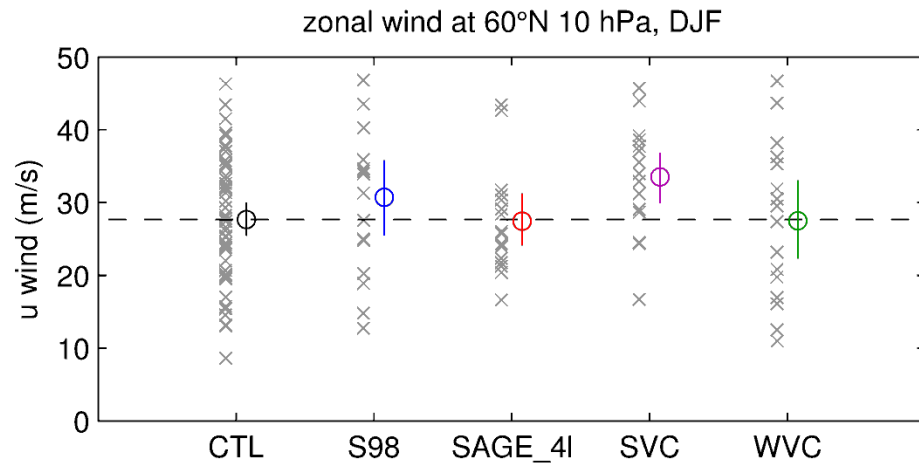
788

789

790 Figure 8: Temperature and zonal wind response of the model-based volcanic forced ensembles. Shown  
 791 are DJF anomalies for the (left) SVC and (middle) WVC ensembles, and (right) the difference between  
 792 the two ensembles for (top) temperature and (bottom) zonal wind. Hatching highlights anomalies which  
 793 are significant at the 95% confidence level based on a bootstrapping algorithm.

794

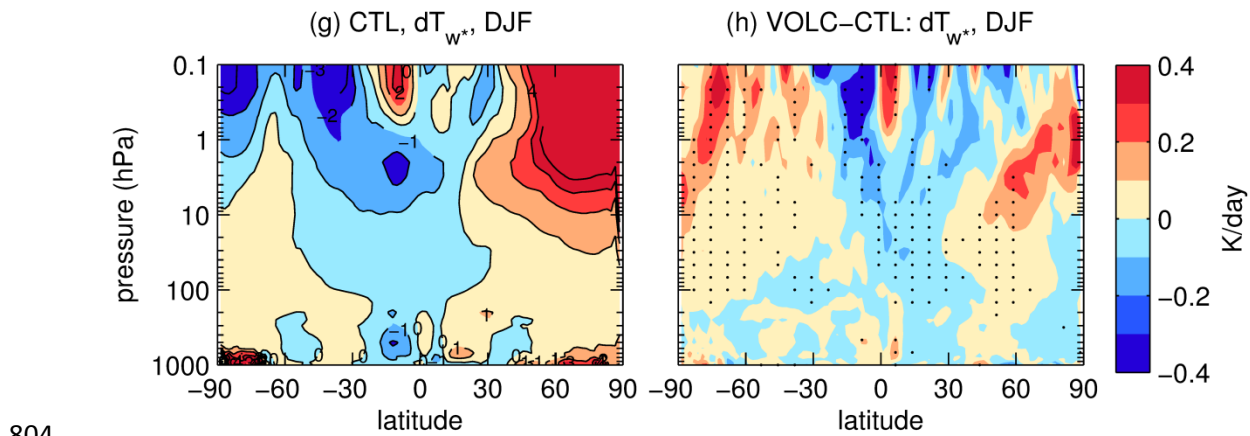
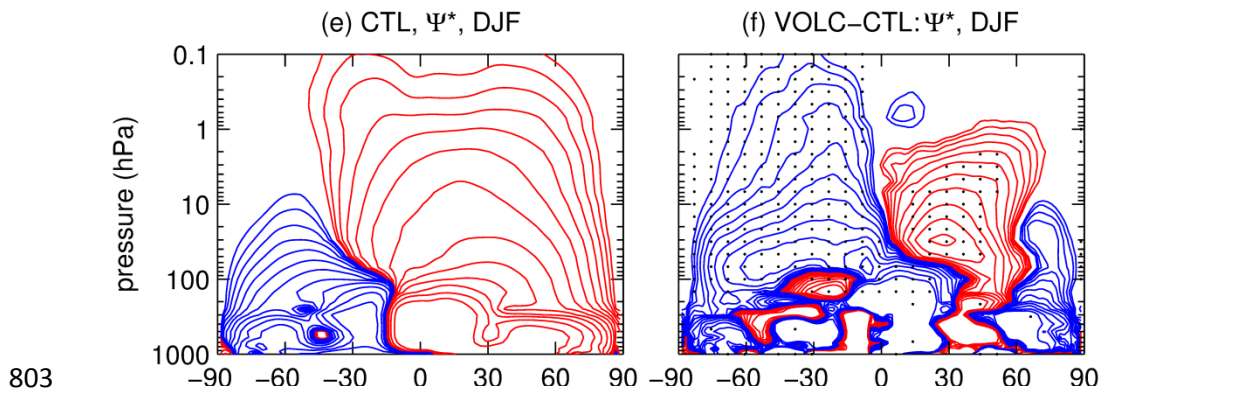
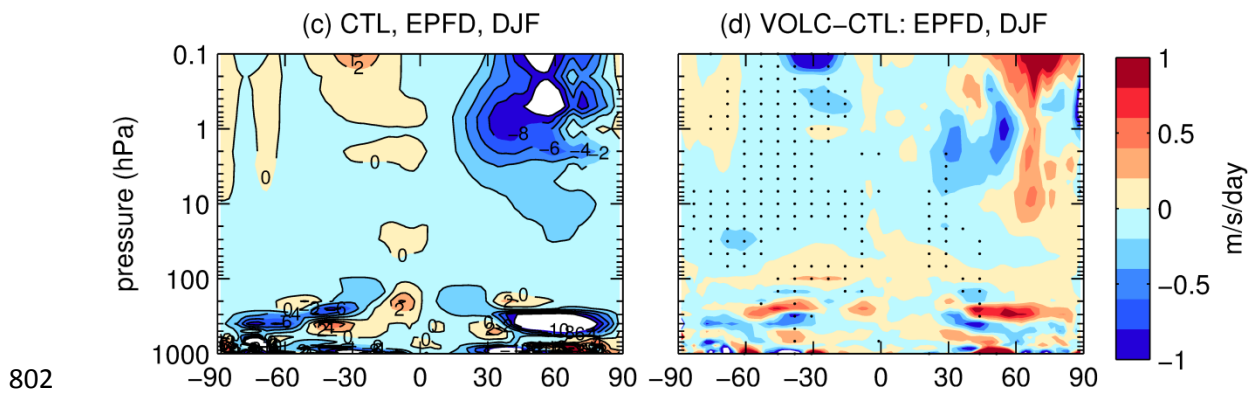
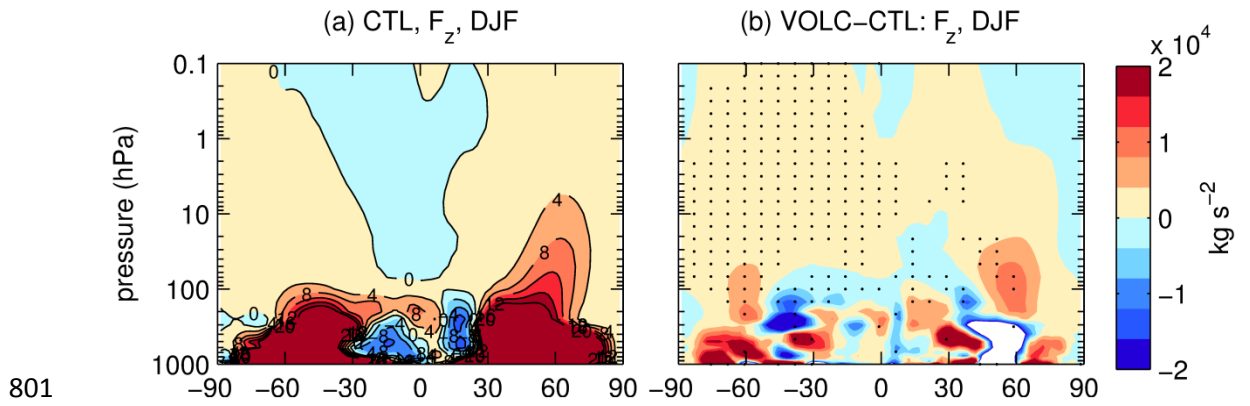




795

796 Figure 9: DJF zonal wind at 60N and 10 hPa for the CTL ensemble and the volcanically forced ensembles  
 797 S98, SAGE\_4λ, SVC and WVC. Individual ensemble members shown as gray symbols. Ensemble means  
 798 shown in colored symbols, with vertical whiskers representing the 95% confidence interval of the  
 799 ensemble mean. Dashed horizontal line shows the ensemble mean of the CTL ensemble.

800

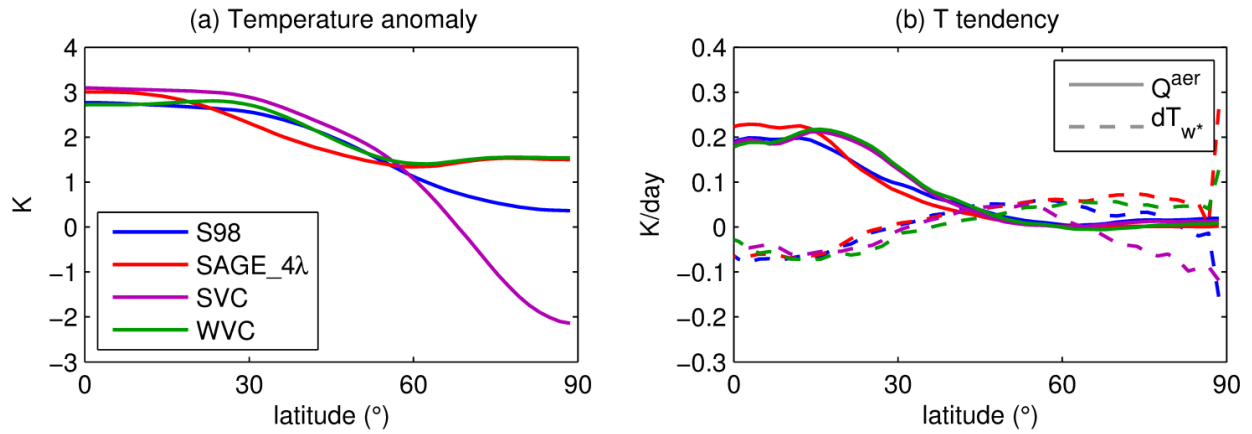


805

806 Figure 10: Selected transformed Eulerian mean diagnostics for the CTL ensemble (left) and anomalies for  
807 the VOLC grand ensemble (right). Shown are (a,b) vertical component of EP-flux, (c,d) EP-flux  
808 divergence, (e,f) residual circulation and (g,h) heating due to residual vertical advection. Contours in (a)  
809 are in units of  $1 \times 10^4 \text{ kg s}^{-2}$ . Stream function contours in (e) and (f) are red for positive values and blue for  
810 negative values, and are log-spaced, ranging from 10 to  $1 \times 10^4 \text{ kg/m/s}$  in panel (e) and 1 to 100  $\text{kg/m/s}$  in  
811 panel (f).

812

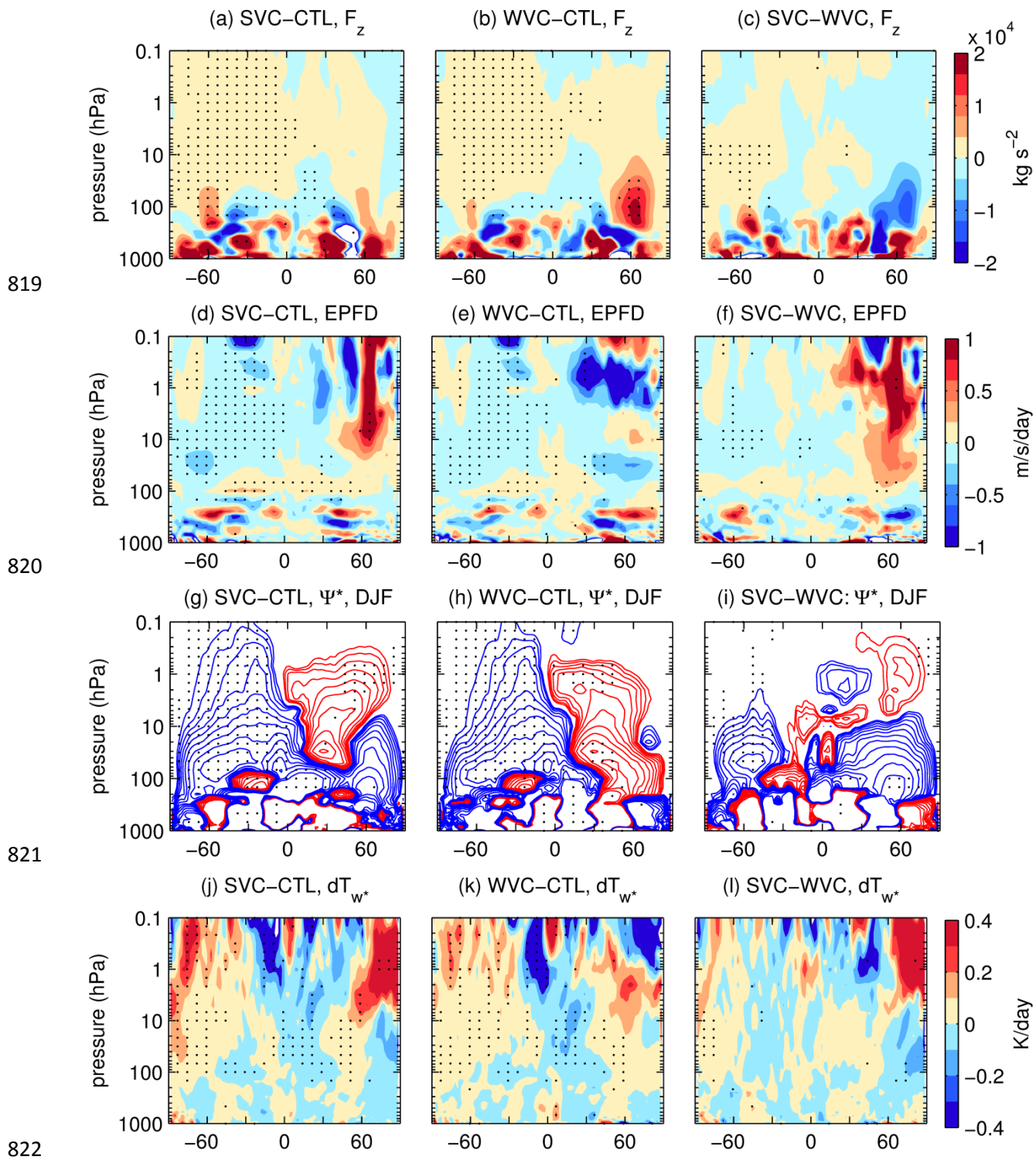
813



814

815 Figure 11: Lower stratospheric (100-20 hPa), DJF average thermodynamic quantities from the S98 and  
 816 SAGE\_4λ forced ensembles: (a) temperature anomalies, (b) temperature tendencies due to aerosol  
 817 radiative heating (solid) and due to vertical advection (dashed).

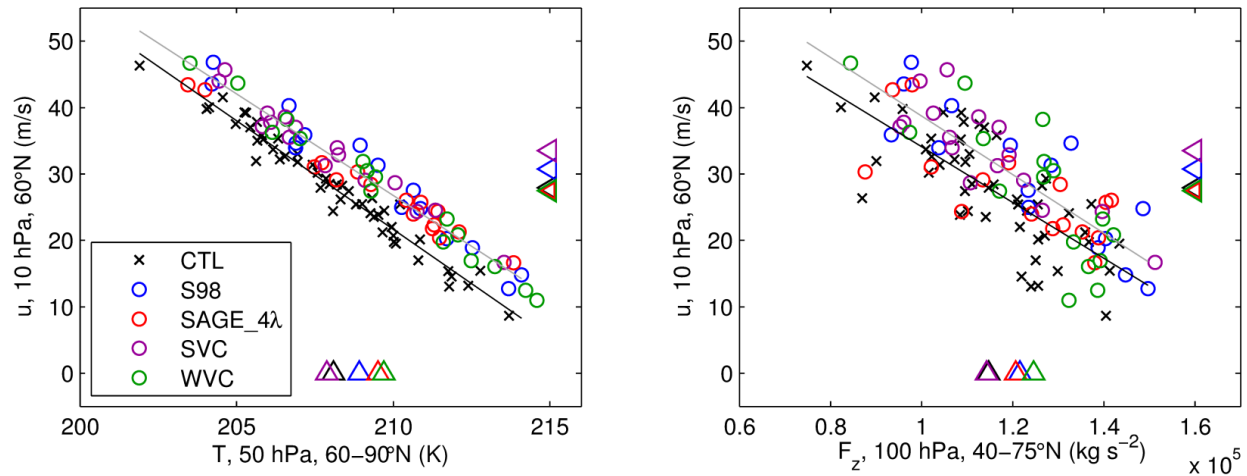
818



823 Figure 12: Selected transformed Eulerian mean diagnostics for the SVC and WVC forced ensembles.  
 824 Shown are DJF anomalies for the (left) SVC and (middle) WVC ensembles, and (right) the difference  
 825 between the two ensembles for (a,b,c) vertical component of EP-flux, (d,e,f) EP-flux divergence, (g,h,i)  
 826 residual circulation and (j,k,l) heating due to residual vertical advection. Stream function contours in

827 panels (g,h,i) are red for positive values and blue for negative values, and are log-spaced ranging from 1  
828 to 100 kg/m/s.

829



830

831 Figure 13: Scatter plots of vortex wind, temperature and wave forcing for the CTL and four volcanically  
 832 forced ensembles. All quantities are averaged over the NH winter (DJF) Shown are (left) zonal wind at 10  
 833 hPa, 60°N plotted against temperature at 50 hPa, 60-90°N averaged, and (right) zonal wind at 10 hPa,  
 834 60°N plotted against the vertical component of EP-flux averaged over 40-75°N. Individual forced  
 835 ensemble members are shown by colored circles, and the CTL ensemble members by black crosses.  
 836 Ensemble mean values of the quantities plotted on the horizontal and vertical axes of each panel are  
 837 shown by colored (black) triangles for the forced (CTL) ensembles along the bottom and right-hand axes.